

# Thermobarometry and geochronology of the Uvauk complex, a polymetamorphic Neoarchean and Paleoproterozoic segment of the Snowbird tectonic zone, Nunavut, Canada<sup>1</sup>

A.J. Mills, R.G. Berman, W.J. Davis, S. Tella, S. Carr, C. Roddick, and S. Hanmer

**Abstract:** The Uvauk complex is an ultramylonite-bounded, granulite-facies suite of anorthosite–gabbro that forms part of the Chesterfield Inlet segment of the Snowbird tectonic zone. Following initial anorthosite–gabbro magmatism at ca. 2.71 Ga and a cryptic 2.62–2.60 Ga event marked by zircon and monazite growth, the Uvauk complex experienced two high-grade tectonometamorphic events at 2.56–2.50 and 1.91–1.90 Ga. Similar to the 2.56–2.50 Ga development of other shear zones in the region, the upper-amphibolite-facies to granulite-facies, moderately high-pressure (8.4–11.0 kbar and 705–760 °C) (1 kbar = 100 MPa) M1 event is interpreted to have involved the structural emplacement of ca. 2.71 Ga Uvauk complex rocks on ca. 2.68 Ga tonalitic rocks to the south. Granulite-facies, high-pressure (11.2–14.7 kbar and 695–865 °C) M2 metamorphism, gabbroic magmatism, and mylonite development within the complex at ca. 1.9 Ga culminated with ~3.5 kbar decompression at high temperature. Clockwise pressure–temperature–time ( $P$ – $T$ – $t$ ) paths reflect crustal thickening, thought to be related to the early accretionary history of the Trans-Hudson Orogen. A thermal overprint at ca. 1.85–1.75 Ga resulted in retrograde metamorphism (5.8–6.0 kbar and 625–695 °C) associated with post-tectonic granitoid plutonism.

**Résumé :** Le complexe d’Uvauk est une suite de gabbro–anorthosite, au faciès des granulites, qui comprend une partie du segment Chesterfield Inlet de la zone tectonique Snowbird; ce complexe est limité par une ultramylonite. Après un magmatisme anorthosite–gabbro initial vers 2,71 Ga et un événement cryptique entre 2,62 – 2,60 Ga marqué par une croissance du zircon et de la monazite, le complexe d’Uvauk a subi deux événements tectonometamorphiques de haut niveau à 2,56 – 2,50 Ga et 1,91 – 1,90 Ga. Semblable au développement d’autres zones de cisaillement dans la région à 2,56 – 2,50 Ga, l’événement M1, au faciès des amphibolites supérieures à celui des granulites et à relativement haute pression (8,4 – 11 kbar et 705 – 760 °C) (1 kbar = 100 Mpa), aurait été impliqué dans la mise en place structurelle des roches Uvauk, ~2,71 Ga, sur les roches tonalitiques au sud, ~2,68 Ga. Le faciès des granulites, un métamorphisme M2 à pression élevée (11,2 – 14,7 kbar et 695 – 865 °C), du magmatisme gabbroïque et le développement de mylonites à l’intérieur du complexe vers 1,9 Ga a culminé avec une décompression d’environ 3,5 kbar à température élevée. Le cheminement des courbes  $P$ – $T$ – $t$  dans le sens horaire est le reflet d’un épaississement possiblement relié à l’histoire accréctionnaire précoce de l’orogène trans-hudsonien. Une surimpression thermique vers 1,85 – 1,75 a causé un métamorphisme rétrograde (5,8 – 6 kbar et 625 – 695 °C) associé à un plutonisme granitoïde post-tectonique.

[Traduit par la Rédaction]

## Introduction

The Snowbird tectonic zone (STZ; Fig. 1) is a geophysical lineament, most distinct on a horizontal gravity gradient map, that extends from Hudson Bay to the foothills of the Rocky Mountains (Walcott and Boyd 1971; Gibb and Halliday 1974). It has been used to divide the western Churchill Province into the Rae and Hearne provinces (Fig. 1)

(Hoffman 1988), here referred to as “domains” (Davis et al. 2000). The significance of the STZ remains controversial, primarily due to conflicting evidence regarding the timing of deformation and metamorphism in deep crustal, granulite-facies rocks in the east Athabasca and Chesterfield segments of the STZ (Fig. 1). The STZ was originally interpreted as a Paleoproterozoic suture zone (Gibb and Halliday 1974; Hoffman 1988), but Hanmer (1997) proposed a ca. 2.6 Ga

Received 19 July 2005. Accepted 10 July 2006. Published on the NRC Research Press Web site at <http://cjles.nrc.ca> on 13 April 2007.

Paper handled by Associate Editor J. Greenough.

**A.J. Mills.** 127 Morrison Drive, Yellowknife, NT X1A 1Z3, Canada.

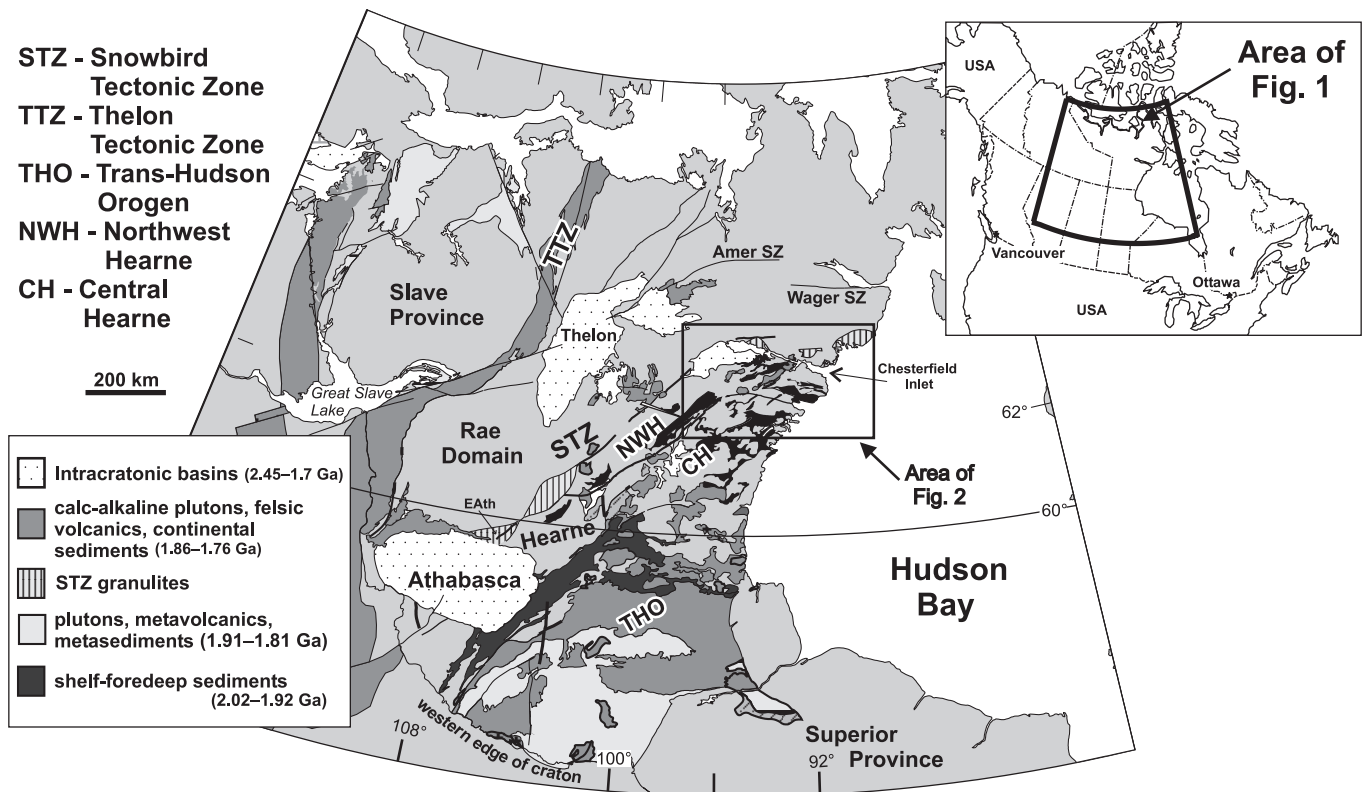
**R.G. Berman,<sup>2</sup> W.J. Davis, S. Tella, C. Roddick, and S. Hanmer.** Geological Survey of Canada, 615 Booth Street, Ottawa, ON K1A 0E8, Canada.

**S. Carr.** Department of Earth Sciences, Carleton University, Ottawa, ON K1S 5B6, Canada.

<sup>1</sup>Geological Survey of Canada Contribution 2005199.

<sup>2</sup>Corresponding author (e-mail: [rberman@nrcan.gc.ca](mailto:rberman@nrcan.gc.ca)).

**Fig. 1.** General geology of the western Churchill Province. EAth, east Athabasca mylonite zone; SZ, shear zone.



intracontinental setting for the east Athabasca segment, northeast of the Athabasca basin (Fig. 1). However, other studies of the segment buried beneath Paleozoic sedimentary rocks in northern Alberta (Ross et al. 1995; Ross and Eaton 2002), the east Athabasca region (Baldwin et al. 2003, 2004; Mahan et al. 2003, 2006; Flowers et al. 2006), and the Chesterfield Inlet segment just west of Hudson Bay (Sanborn-Barrie et al. 2001) have highlighted the importance of Paleoproterozoic (ca. 1.9 Ga) events along these portions of the STZ (Fig. 1).

This study focuses on the Uvauk complex (Tella et al. 1993, 1994; Mills 2001), one of a number of high-grade complexes along the Chesterfield Inlet segment of the STZ (Fig. 2) that share similar lithologic, structural, and metamorphic features. Others include the Daly Bay complex (Gordon 1988; Hanmer and Williams 2001), the Kramanituak complex (Sanborn-Barrie et al. 2001), the Hanbury Island shear zone (Tella and Annesley 1988), and disparate anorthosite exposures on Walrus and Coats islands (Schau 1991). In this region (Fig. 2), the STZ potentially forms one boundary of the northwestern Hearne subdomain (Davis et al. 2006), which is distinguished from the central Hearne subdomain (Fig. 2) by the occurrence of younger granitic rocks (ca. 2.6 Ga) and tectonometamorphism (ca. 2.56–2.50 Ga). Here we present new thermobarometric and U–Pb geochronology data that reveal strong parallels with the Kramanituak complex (Sanborn-Barrie et al. 2001) and provide further insight into the evolution of this portion of the STZ.

## Geology of the Uvauk complex

In map view, the Uvauk complex is approximately 30 km

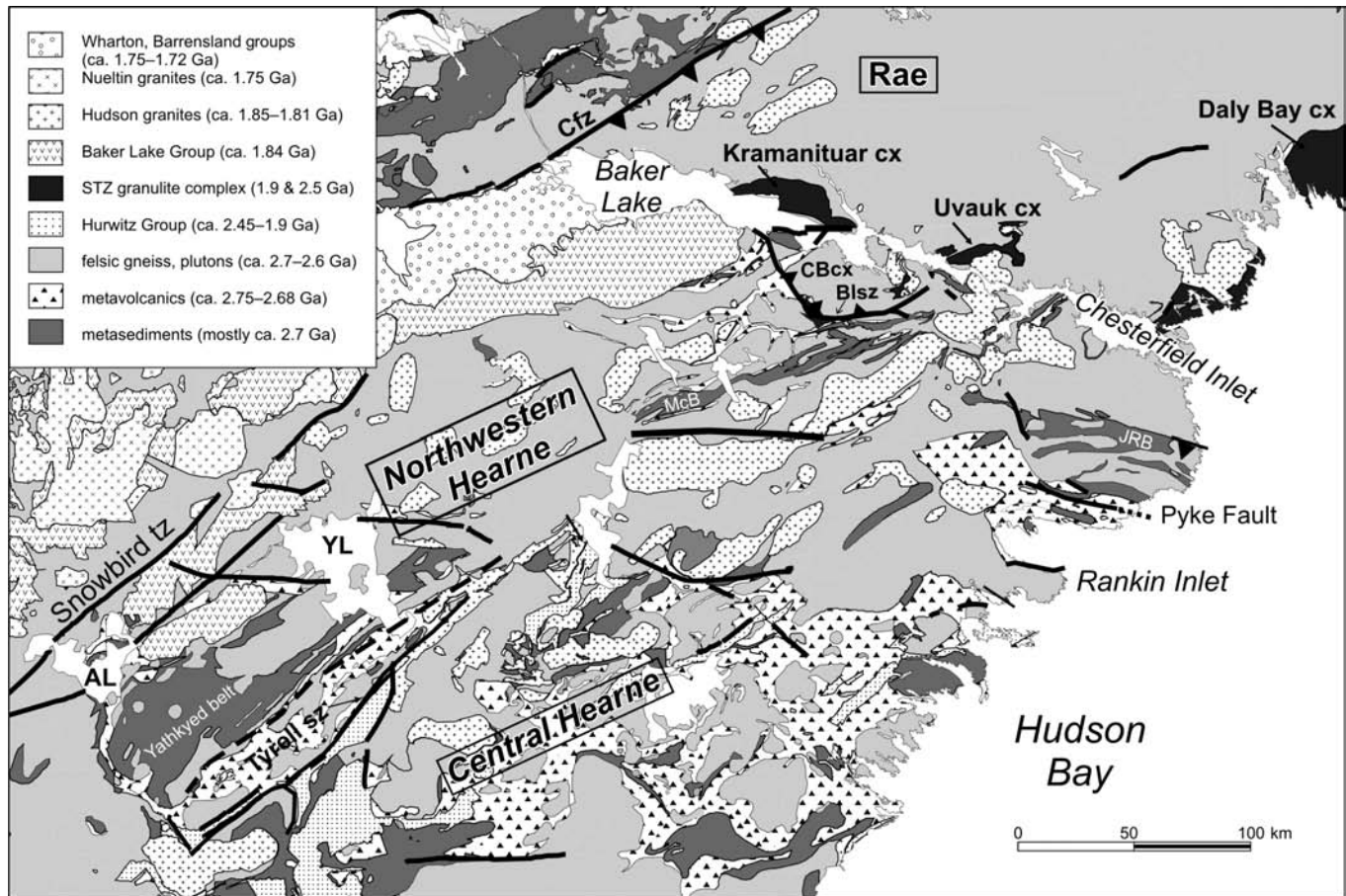
long and varies from ~20 km wide at the easternmost part of the complex to ~1 km at the westernmost part, near Uvauk Inlet (Fig. 2). The primary geometry of the Uvauk complex is that of a folded sheet (Tella and Schau 1994) that structurally overlies predominantly tonalitic country rocks. In the west, rocks of the complex (Fig. 3) dip steeply to the south, but at the eastern extremity of the complex they dip gently to the west. The westernmost part of the complex represents a tightly folded, east-plunging synform, whereas the eastern part is characterized by open, upright, east–west-trending and north- to north-northwest-trending folds and minor dome and basin interference structures. Contacts between anorthosite in the complex and the surrounding country rocks are everywhere concordant; no crosscutting relations were observed. Amphibolite-facies mineral assemblages (both prograde and retrograde) are prevalent, but granulite-facies assemblages are locally preserved.

This study focuses on the western part of the Uvauk complex, which consists of a package of metamorphosed and sheared composite, metaigneous (mafic–anorthositic) rocks. The complex is bounded by two east-striking “northern” and “southern” shear zones (Fig. 3), which are described in the section following that of the lithology of the complex and country rocks.

## Anorthosite suite

The anorthosite suite is dominated by white-weathering, plagioclase-rich rocks with <10% clinopyroxene commonly rimmed or replaced by hornblende. Gabbroic anorthosite is most common in the core of the suite. The southernmost part is coarse-grained (~2–10 cm pyroxene) anorthositic gabbro

**Fig. 2.** Regional geological setting of the Chesterfield Inlet segment of the Snowbird tectonic zone. AL, Angikuni Lake; Blsz, Big Lake shear zone; CBcx, Cross Bay complex; Cfz, Chesterfield fault zone; cx, complex; JRB, Josephine River belt; McB, MacQuoid belt; sz, shear zone; tz, tectonic zone; YK, Yathkyed Lake.



to leucogabbro. At the northern margin of the suite, predominant garnet-bearing anorthosite is locally intercalated with garnet-free anorthosite, suggesting intrusion of different phases of anorthosite magmas.

The anorthosite suite contains an east-striking, steeply south-dipping, variably developed foliation ( $\sim 079^\circ/77^\circ\text{S}$ ) and a well-developed, east-plunging extension lineation ( $\sim 43^\circ \rightarrow 080^\circ$ ). Anorthositic gabbro that cores the Uvauk complex occurs either as heterogeneously sheared, internally boudinaged mylonite or as homogeneously deformed, flaser-textured panels, reflecting either an age difference between two distinct anorthosite units or strain partitioning.

#### Mafic granulite dykes

Fine-grained, black, granulite-facies metagabbro dykes make up nearly 40% of the anorthosite suite (Fig. 4a). The dykes range in width from tens of centimetres in the north to  $\sim 50$  m in the south and typically contain clinopyroxene–orthopyroxene–garnet–plagioclase with retrograde hornblende. A penetrative foliation concordant with dyke margins and foliation in the host anorthosite is common. The dykes were emplaced late in the deformational history of the Uvauk complex based on local preservation of rare chilled margins (Fig. 4b), bayonet-like apophyses (Fig. 4c), low-angle contacts where undeformed dyke margins crosscut mylonitic foliation in anorthosite, and the occurrence of some dykes that

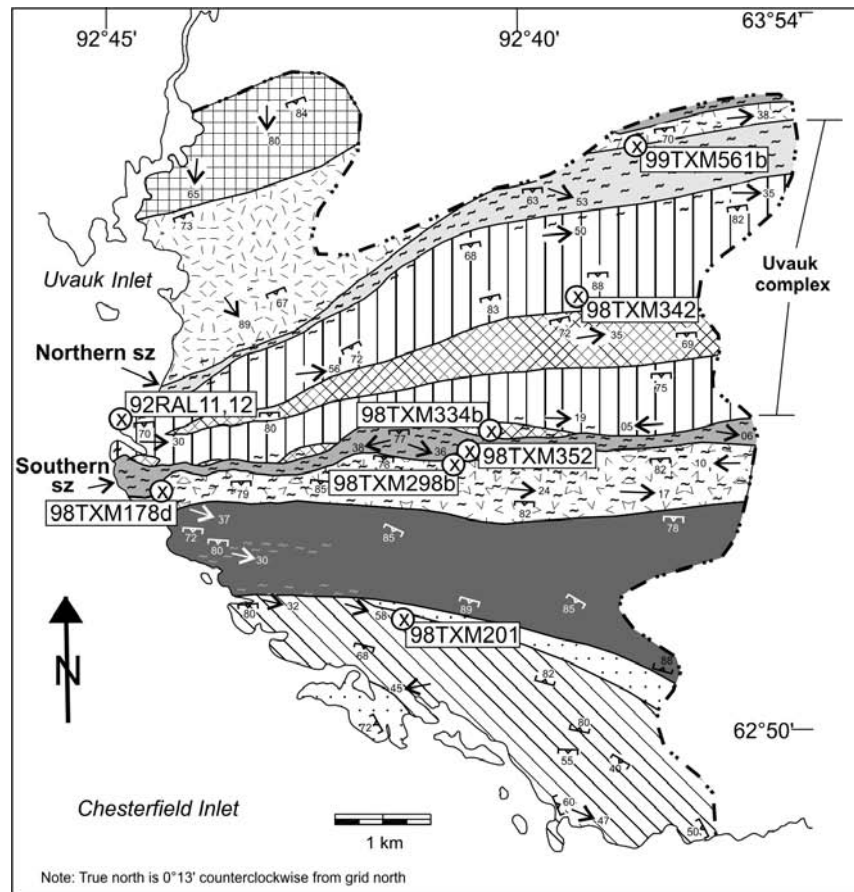
crosscut both the regional foliation and other deformed dykes (Fig. 4d). These relationships demonstrate that dyke emplacement was broadly synchronous with, and outlasted, anorthosite deformation and likely represented a significant heat source during deformation and metamorphism of the Uvauk complex. Some gabbro dykes are boudinaged, whereas at the western end of the complex (Fig. 3) others are isoclinally folded along with the anorthosite (Fig. 4e). An axial planar foliation, defined by aligned hornblende enveloping garnet pseudomorphs (Fig. 4f), is particularly well developed in fold hinges within the folded dykes. The anorthosite exhibits an older mylonitic foliation that is folded (Fig. 4e), however, possibly indicating an earlier episode of anorthosite deformation prior to gabbro dyke intrusion.

#### Southern country rocks

Outcrops south of the anorthosite suite are dominated by grey, medium-grained, biotite  $\pm$  hornblende-bearing, tonalite orthogneiss with abundant concordant lenses of amphibolite and semipelitic schist. Lithologic similarities suggest that the tonalite orthogneiss represents an extension of the MacQuoid belt (Tella et al. 1993) that occurs southwest of Chesterfield Inlet (Fig. 2). White, coarse-grained hornblende tonalite is generally concordant with, but locally crosscut by, biotite–tonalite orthogneiss. The biotite–tonalite orthogneiss is flanked to the southwest by foliated, garnet–biotite schist,



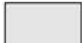


**Fig. 3.** Geology of the western Uvauk complex, showing representative structural elements and sample locations referred to in the text. sz, shear zone.




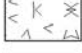


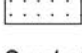


### LEGEND

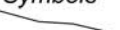

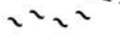


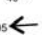
#### Anorthosite Suite

-  Anorthosite (60%), mafic granulite dykes (40%)
-  Variably deformed anorthositic gabbro, leucogabbro, and mafic granulite
-  Well banded marginal garnet-anorthosite and mafic granulite

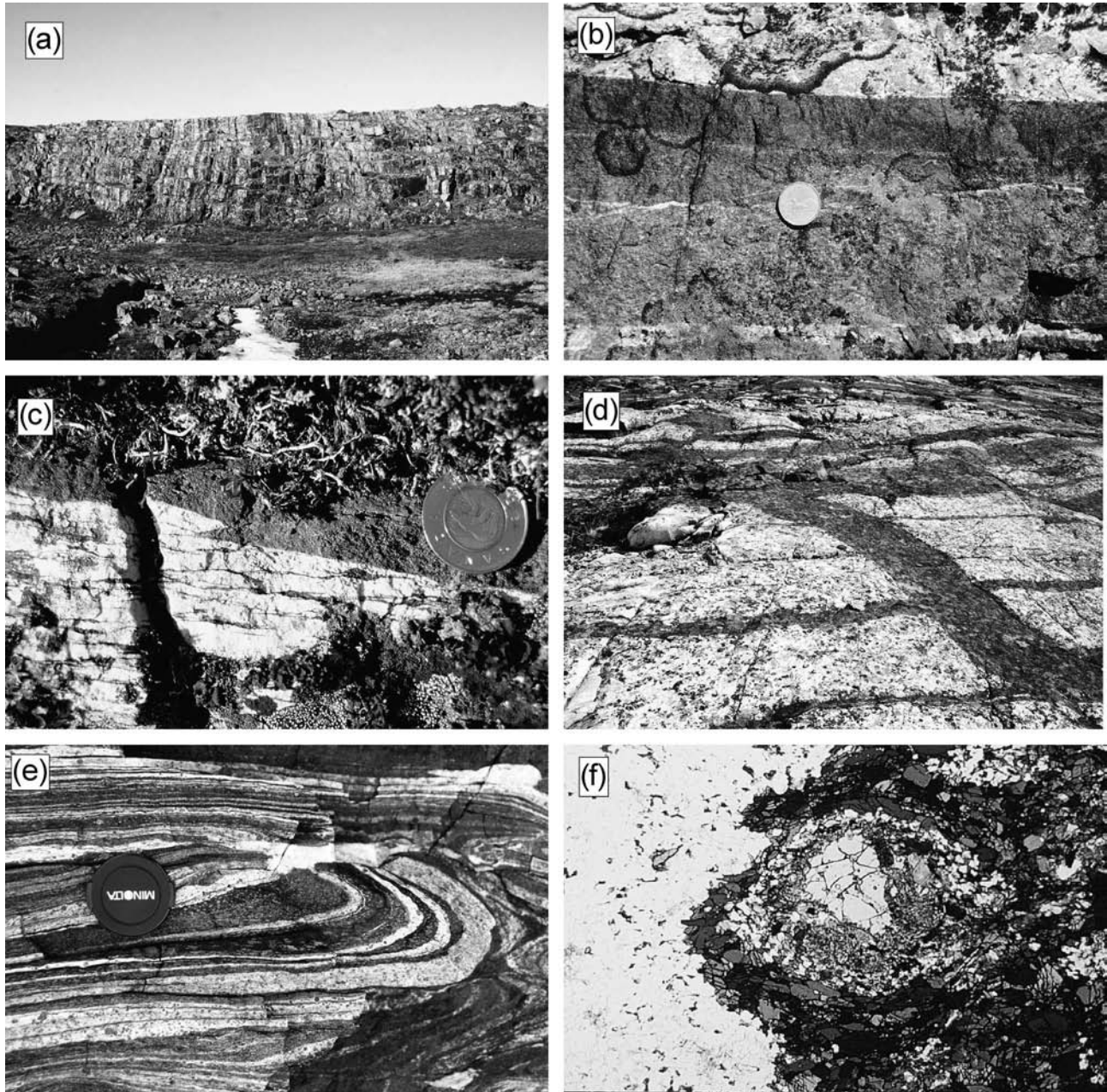
#### Surrounding Geology (relative ages unknown)

-  Moderately foliated, well lineated, tonalite with inclusions of mafic granulite and pyroxenite
-  Well-banded biotite–hornblende–tonalite, minor pink augen granodiorite, amphibolite, and biotite-schist
-  Green to grey, diorite straight gneiss, minor garnet–quartzofeldspathic gneiss, tonalite gneiss, and amphibolite
-  Buff to tan, garnet–quartzofeldspathic gneiss, minor tonalite gneiss, and amphibolite
-  White to grey, hornblende–biotite–tonalite straight gneiss with minor clinopyroxenite and paragneiss
-  Grey biotite–tonalite orthogneiss with subordinate white hornblende–tonalite and amphibolite
-  Buff to rust, plagioclase–porphyroblastic, garnet–semipelitic schist, minor granoblastic amphibolite, and tonalite

#### Symbols

-  Lithological contact
-  Limit of mapping
-  Shear zone rocks
-  Sample location
-  Foliation
-  Lineation

**Fig. 4.** Dykes within the Uvauk complex. (a) East-trending, fine-grained, generally concordant, granulite-facies mafic dykes that make up nearly 40% of the metagneous suite by volume (view looking east). (b) Rare chilled margins confirm the mafic layers in (a) are dykes. Coin for scale. (c) Preservation of bayonette-like apophyses and obliquity of dyke margins to the anorthosite foliation imply late-stage dyke emplacement. Coin for scale. (d) One dyke crosscuts regional fabrics and similar dykes, suggesting that dyke emplacement outlasted deformation. (e) Layers of anorthosite and mafic granulite dyke isoclinally folded: foliation within the anorthosite is folded, whereas the dyke has a weakly developed foliation that is axial planar to the fold. Lens cap for scale. (f) The weak axial planar foliation in mafic bands of (e) is defined by elongate garnet pseudomorphs and aligned hornblende that wrap the pseudomorphs (axial plane is parallel to width of photomicrograph; field of view is 5.2 mm).



with intercalated amphibolite and garnet–amphibolite. All southern country rocks are well foliated to gneissic, with an average planar foliation of  $109^{\circ}/66^{\circ}\text{SW}$  and a mean extension lineation of  $40^{\circ} \rightarrow 121^{\circ}$ . Rare shear-sense indicators show dominantly dextral shear sense (Mills 2001), but sinistral shear-sense indicators are also present (Tella et al. 1993).

Increasingly strained rocks occur north of the tonalite ortho-

gneiss. White to light grey, medium-grained tonalite “straight gneiss” contains 10–30 cm wide compositional bands extending along strike for >50 m. Garnet-quartzofeldspathic gneiss is also well banded, with millimetre-scale melanocratic bands alternating with centimetre-scale leucocratic bands. Directly south of the anorthosite suite, homogeneous, clinopyroxene–orthopyroxene-bearing dioritic to monzodioritic, ultramylonite



gneiss is intercalated with the quartzofeldspathic gneiss. A plutonic protolith is suggested by igneous textures preserved in rare low-strain pods.

### Northern country rocks

Immediately north of the anorthosite, grey, medium-grained, well-banded hornblende–biotite tonalite gneiss contains abundant 2–10 cm thick, conformable amphibolite layers and local garnet–amphibolite inclusions. Farther north, white to grey, medium-grained, foliated biotite  $\pm$  orthopyroxene tonalite occurs in topographic lows between more resistant, ~50–100 m diameter enclaves of dark green, fine- to medium-grained, mafic granulite and pyroxenite. These are interpreted as large xenoliths or rafts within the tonalite. White to pink, strongly lineated enderbite intruded and brecciated the mafic granulite and pyroxenite. Most northern country rocks exhibit a moderately developed, northeast-striking foliation (mean = 060°/75°SSE) and a downdip lineation (mean = 75°  $\rightarrow$  149°).

### Southern shear zone

The southern boundary of the southern shear zone is marked by a strain gradient, involving a northward reduction in grain size and an increase in the ratio of matrix to porphyroclast. Anorthositic gabbro and leucogabbro rocks in the shear zone contain spectacular clinopyroxene ribbons with aspect ratios up to 10:1 and a plagioclase-rich matrix that is nearly 100% recrystallized to produce a foam texture characteristic of rocks deformed and annealed at high temperature (Hanmer 2000). The mean foliation within the shear zone is oriented at 091°/79°S. Lineations plunge shallowly to the east and west, although it is unclear if this reflects two generations of lineation or one generation that varies about the horizontal. Shear-sense indicators yield dextral shear sense (Mills 2001). The presence of a systematic strain gradient on the north side of the shear zone could not be demonstrated due to the heterogeneous state of strain and lack of outcrop.

### Northern shear zone

The east-northeast-trending northern shear zone is ~500–1000 m wide and dominantly consists of well-banded anorthosite–gabbro ultramylonite, with a mean foliation of 067°/71°SE and mean extension lineation of 57°  $\rightarrow$  090°. Shear-sense indicators are mostly sinistral, but dextral indicators are also present. One outcrop of garnet-bearing quartzofeldspathic gneiss and a ~50 m thick panel of diorite gneiss are similar to those of the southern shear zone and described earlier in the paper, suggesting repetition of map units within a synform at the western end of the Uvauk complex (Tella et al. 1993). Approaching the northern shear zone from the south, a strain gradient is evident from the increase in (i) the aspect ratio of flattened mafic grains, (ii) the apparent attenuation of mafic dykes, and (iii) the ratio of matrix to porphyroclast. Rocks within the northern shear zone display a strong banding, with rare rootless intrafolial folds, that is absent in amphibolitic rocks north of the northern shear zone.

## Thermobarometry

### Methods

Microprobe analyses of metamorphic minerals were obtained at the Geological Survey of Canada using routine techniques (e.g., Berman et al. 2005). The thermobarometry with estimation of equilibration state (TWEEQU) software multi-equilibrium approach (Berman 1991) was used for pressure–temperature ( $P$ – $T$ ) calculations. The following set of independent equilibria was used in this study. Equilibria (thermometers 1–7; barometers 8–12) are written with the higher- $T$  assemblage on the right (mineral abbreviations from Kretz 1983), where aOk = Al<sub>2</sub>O<sub>3</sub> component of orthopyroxene (orthocorundum; Ts, Mg-tschermakite):

- [1] Alm = aOk + 3Fsl
- [2] En + 2Alm = 3Fsl + 2Prp
- [3] Alm + 3Di = Prp + 3Hd
- [4] 3Tr + 5Alm = 5Prp + FeTr
- [5] Alm + Phl = Prp + Ann
- [6] Ed + Ab = Ri + An
- [7] Ed + 4Qtz = Tr + Ab
- [8] 3Qtz + 2Grs + Alm = 3An + 3Hd
- [9] 3Qtz + Grs + 2Alm = 3An + 6Fsl
- [10] 12Qtz + 3Ts + 2Prp + 4Grs = 12An + 3Tr
- [11] Grs + 2Ky + Qtz = 3An
- [12] Grs + Qtz + 2Rt = 2Ttn + An

All thermobarometric calculations, with the exception of equilibria [1], [6], and [7], were computed using TWEEQU version 1.02 (Geological Survey of Canada, Ottawa), which incorporates the Berman (1990), Fuhrman and Lindsley (1988), McMullin et al. (1991), Newton (1983), and Mäder et al. (1994) activity models for garnet, plagioclase, biotite, pyroxene, and amphibole, respectively. The Al in Opx thermometer (equilibrium [1]) of Aranovich and Berman (1997) was calculated using the TWEEQU version 2.02 with thermodynamic data of Berman and Aranovich (1996). The use of TWEEQU version 2.02 does not introduce significant error because differences in thermodynamic parameters of orthopyroxene and garnet in the two versions of TWEEQU are small. Amphibole thermometry based on equilibria [6] and [7] (Holland and Blundy 1994) was generally preferred to Fe–Mg garnet–amphibole exchange thermometry with equilibrium [4] because of large uncertainties in estimated Fe<sup>3+</sup> in amphibole. Equilibrium [6] was used for anorthositic rocks because it does not require the presence of quartz and is recommended for high-temperature samples with anorthite-rich feldspars and low silica activity (Holland and Blundy 1994). Equilibrium [7] was used for silica-saturated samples.

### Results

Three main metamorphic events are interpreted from petrographic textures and  $P$ – $T$  results for 14 samples of the western map area (12 from Mills 2001 and two from reconnaissance

analyses reported by Tella et al. 1994). We refer to these events as M1, M2, and M3, with M2 divided into an early phase (M2a) corresponding to near-peak *P*, and in some cases associated with peak *T*, and a later decompressional phase (M2b). Representative results (Table 1; Fig. 5) for four samples that best constrain the granulite-facies M1 and M2 events are summarized in the following four sections. We do not present details of the retrograde M3 event (5.8–6.0 kbar (1 kbar = 100 MPa) and 625–695 °C), which is best recorded in semipelitic schist and amphibolite south of the Uvauk complex (Mills 2001).

We note that retrieval of quantitative *P–T* values is challenging for rocks that have experienced a high-grade polymetamorphic history. Because of the possibility of reequilibration of M1 compositions during M2, *P–T* values derived for M1 conditions should be considered as estimates. *P–T* values derived from rim and near-rim compositions for M2a and M2b are considered most reliable, but the possibility that M2 results are compromised by intersection of equilibria with different closure temperatures cannot be ruled out (e.g., Aranovich and Berman 1997). The high temperatures retrieved for M2 and the good agreement between the Fe–Mg exchange and Al in Opx net transfer thermometers for Opx-bearing rocks (see later in the paper; and Mills 2001), however, indicate that the mineral compositions selected for thermobarometry were not strongly affected by retrograde cation exchange.

#### **Sample 98TXM342: mafic dyke**

A ~30 m wide mafic dyke within the anorthosite suite contains ~35% garnet, 35% clinopyroxene, 25% plagioclase, <5% quartz, minor orthopyroxene and hornblende, and trace ilmenite. Relict 100 µm wide orthopyroxene is present and is generally mantled by clinopyroxene up to ~500 µm in diameter. Hornblende is generally restricted to narrow zones (~1 mm) near microfractures. Garnet forms equant to elongate, ~0.5–1.0 mm diameter porphyroblasts that are interpreted as syntectonic because they both truncate and are enveloped by the mylonitic foliation, defined by elongate aggregates of clinopyroxene and plagioclase (Fig. 5a).

Continuous core–rim chemical zoning in sample 98TXM342 (Fig. 5a) is interpreted to have formed during a single metamorphic event, designated as M2 on the basis of regional correlations presented in the Discussion section. Fe/(Fe + Mg) in garnet increases from core (0.60–0.62) to rim (0.67–0.68), and CaO in garnet decreases from core ( $X_{\text{Grs}} = 0.23\text{--}0.25$ ) to rim ( $X_{\text{Grs}} = 0.20\text{--}0.18$ ). Plagioclase compositions are uniform ( $\text{An}_{40\text{--}50}$ ) but may increase in anorthite content toward garnet. Orthopyroxene with Fe/(Fe + Mg) between 0.43 and 0.48 is rimmed by clinopyroxene (Fig. 5a), with minor hornblende. Because the mantling of orthopyroxene by clinopyroxene allows the possibility that orthopyroxene may be a relic igneous phase, *P–T* results are based on clinopyroxene, using equilibria [3] and [8] (Fig. 5a). Interpreted near-peak (M2a) *P–T* conditions of 12.7 kbar and 870 °C, based on the average of four different microdomains, are derived from core compositions of garnet and matrix clinopyroxene and plagioclase located 200–500 µm from garnet. Rim compositions yield M2b conditions of 8.8 kbar and 775 °C,

based on the average of three microdomains. As the isopleths for both equilibria [3] and [8] are shifted for rim relative to core compositions, these conditions are interpreted to represent a valid point on the decompressive part of a clockwise *P–T* path, not a spurious product of Fe–Mg reequilibration without operation of net transfer reaction [8].

#### **Sample 99TXM561b: garnet leucogabbro**

Well-foliated garnet leucogabbro within the northern shear zone exhibits foliation-parallel compositional banding defined by plagioclase- and hornblende-rich layers. The modal mineralogy is 50% plagioclase, 30% garnet, 10% hornblende, 6% titanite, 2% quartz, and 1%–2% clinopyroxene, ilmenite, and rutile. Clinopyroxene, up to ~200 µm in size, is generally rimmed by hornblende. Subhedral, highly fractured garnet porphyroblasts, containing abundant inclusions of plagioclase, hornblende, titanite, ilmenite, quartz, and rare rutile, are enveloped by the foliation and surrounded by ~1 mm wide hornblende coronae or hornblende–plagioclase symplectite (Fig. 5b).

Large garnet porphyroblasts up to 2 cm in diameter are characterized by low-CaO cores ( $X_{\text{Grs}} = 0.23\text{--}0.27$ ), with 500–750 µm wide, markedly higher CaO rims (increasing rimward from  $X_{\text{Grs}} = 0.35$  to  $X_{\text{Grs}} = 0.49$ ) that are best preserved where hornblende–plagioclase symplectite is not well developed. Where hornblende–plagioclase symplectite is well developed (Fig. 5b),  $X_{\text{Grs}}$  does not exceed ~0.37 in Grt rims and Fe/(Fe + Mg) decreases slightly from core (0.78–0.81) to rim (0.77–0.78).  $X_{\text{Sps}}$  is also slightly elevated in the core (~0.04) relative to the rim (~0.008). Amphibole varies from tschermakite inclusions in garnet, tschermakite–edenite grains in well-developed symplectite, and hornblende to actinolitic hornblende in poorly developed symplectite. Matrix plagioclase is ~ $\text{An}_{48\text{--}53}$ . Symplectite plagioclase compositions are more calcic and more heterogeneous ( $\text{An}_{67\text{--}82}$ ). In general, unzoned plagioclase inclusions are abundant within garnet porphyroblasts. Inclusions within the low-CaO garnet core vary between  $\text{An}_{42}$  and  $\text{An}_{48}$  (Fig. 5b). Two ~200 µm diameter unzoned inclusions within the high-CaO garnet rim indicate an outward increase in  $X_{\text{An}}$  ( $\text{An}_{58\text{--}70}$ ). The CaO increase in both plagioclase and garnet is likely due to titanite breakdown to rutile, which occurs in the high-CaO garnet rims.

Three sets of *P–T* conditions were calculated (Fig. 5b). The low-CaO garnet core and a composite hornblende (~50 µm) and plagioclase (~200 µm) inclusion yield 11.3 kbar and 760 °C. These results are interpreted to represent M1 conditions, with the garnet rim yielding M2 conditions similar to those derived from sample 98TXM342. Maximum *P–T* (M2a) conditions of 14.7 kbar and 790 °C derive from the compositions of the inner garnet rim with plagioclase and hornblende inclusions located near the core–rim boundary. Late-stage *P–T* (M2b) conditions of 10.0 kbar and 800 °C were derived from the compositions of high-CaO garnet rim and adjacent symplectitic plagioclase and hornblende.

#### **Sample 98TXM178d: quartzofeldspathic gneiss**

Strongly foliated and lineated quartzofeldspathic gneiss of the southern shear zone consists of ~30% garnet, 40% plagioclase, 20% quartz, 5% biotite, <5% orthopyroxene or cummingtonite (the two are mutually exclusive), and trace

**Table 1.** Mineral chemistry and *P–T* results.

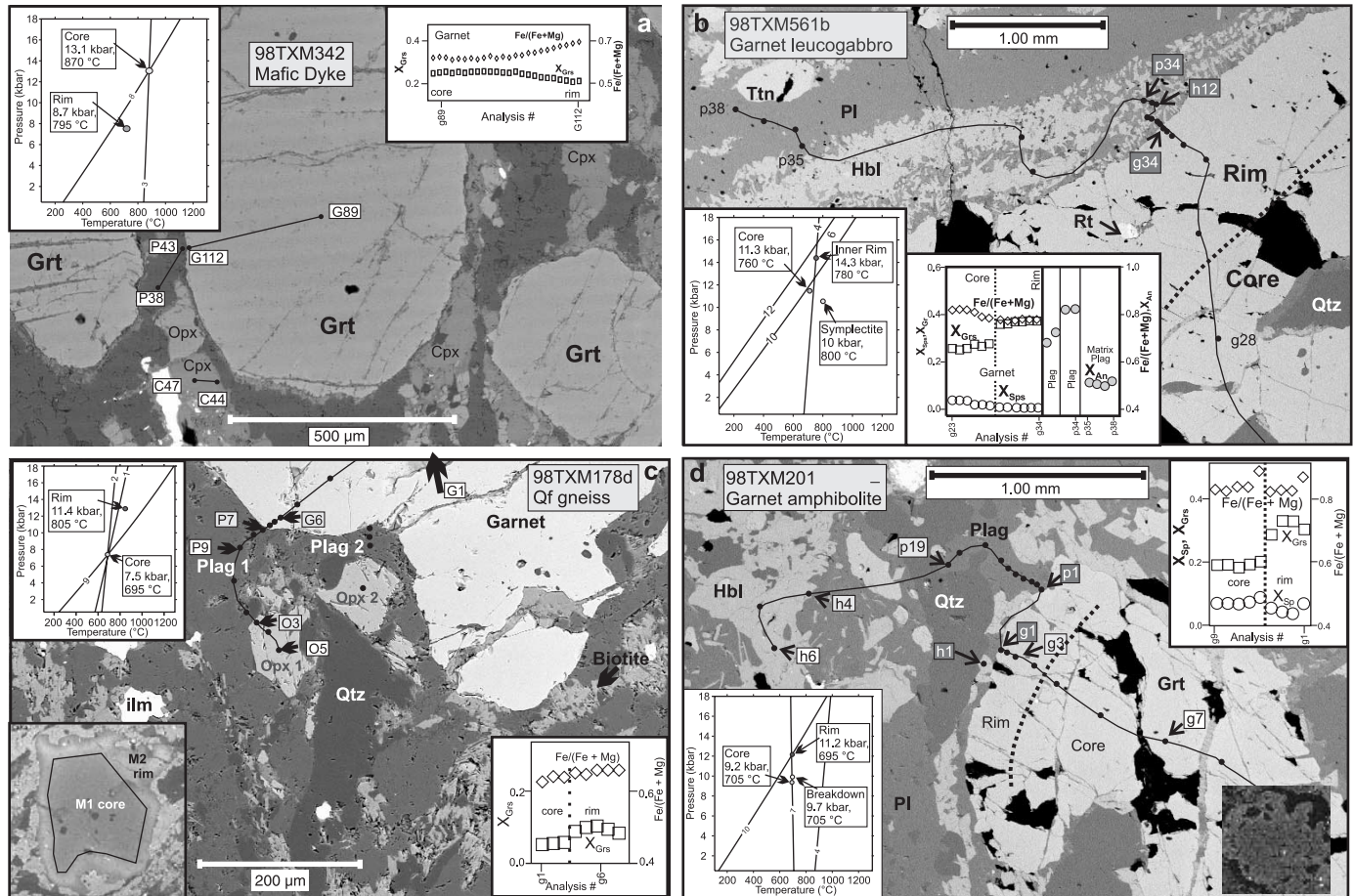
(A) Sample No.:	561b-M1			561b-M2a			561b-M2b			342-M2a				342-M2b			
Analysis No.:	G14	P16	H4	G14'A	P4'A	H6B	G12H	P5H	H5H	G1	P7	C6	O3	G8	P2	C2	O2
Mineral:	Grt	Pl	Hbl	Grt	Pl	Hbl	Grt	Pl	Hbl	Grt	Pl	Cpx	Opx	Grt	Pl	Cpx	Opx
Analysis site:	Core	Core	Core	Rim	Rim	Rim				Core				Rim	Rim	Rim	Rim
Assemblage:	B	B	B	A	A	A	H	H	H	A	A	A	A	B	B	B	B
SiO <sub>2</sub> (wt.%)	37.7	56.0	39.6	37.5	51.5	39.1	37.8	46.2	40.5	38.4	57.9	50.4	50.7	38.5	53.4	50.6	50.5
TiO <sub>2</sub>	0.2	nd	0.4	0.3	nd	0.5	0.4	nd	0.7	0.1	nd	0.3	0.1	0.1	nd	0.5	0.1
Al <sub>2</sub> O <sub>3</sub>	20.8	27.4	16.9	20.1	29.3	17.4	19.0	34.4	12.6	21.8	26.7	2.8	1.5	21.5	28.2	3.8	1.8
Cr <sub>2</sub> O <sub>3</sub>	0.0	nd	0.0	0.0	nd	0.0	0.0	nd	0.0	0.0	nd	0.1	0.1	0.0	nd	0.0	0.1
FeO	26.9	0.1	18.1	19.8	0.2	17.6	22.3	0.1	24.2	21.5	0.1	9.5	26.8	25.1	1.0	9.8	27.7
MnO	1.5	nd	0.2	0.3	nd	0.2	0.5	nd	0.1	0.5	nd	0.1	0.3	0.8	nd	0.1	0.3
MgO	3.4	nd	7.6	2.5	nd	7.3	1.2	nd	4.4	7.8	nd	12.9	18.9	6.7	nd	12.7	18.2
CaO	9.6	9.7	11.3	18.5	12.4	11.4	18.2	17.8	11.6	8.5	8.4	21.0	0.3	6.5	10.9	21.1	0.6
Na <sub>2</sub> O	0.0	5.7	1.9	0.0	4.9	1.9	0.0	1.5	1.4	0.0	6.4	0.5	0.0	0.0	4.5	0.5	0.0
K <sub>2</sub> O	0.0	0.1	0.4	0.0	0.0	0.4	0.0	0.0	0.2	0.0	0.1	0.0	0.0	0.0	0.1	0.0	0.0
Total	100.1	99.0	96.4	99.0	98.4	96.1	99.4	100.1	95.7	98.7	99.6	97.6	98.6	99.2	98.0	99.0	99.1
<i>P–T</i> estimates	11.3 kbar, 760 °C			14.3 kbar, 780 °C			10.0 kbar, 800 °C			13.1 kbar, 870 °C				8.7 kbar, 790 °C			

(B) Sample No.:	178d-M1			178d-M2a			201-M1			201-M2a			201-M2b		
Analysis No.:	G6	P4	O3	G6	P7	O3	G13	P15C	H9	G4C	P12C	H8C	G1G	P1G	H1G
Mineral:	Grt	Pl	Opx	Grt	Pl	Opx	Grt	Pl	Hbl	Grt	Pl	Hbl	Grt	Pl	Hbl
Analysis site:	Core	Core	Core	Rim	Rim	Rim	Core	Core	Core	Rim	Rim	Rim			
Assemblage:	A	A	A	C	C	C	C	C	C	C	C	C	G	G	G
SiO <sub>2</sub> (wt.%)	39.5	62.2	52.1	38.7	62.1	53.4	36.7	60.2	41.2	37.3	60.9	40.9	38.0	58.5	41.4
TiO <sub>2</sub>	0.1	nd	0.1	0.1	nd	0.1	0.0	nd	1.1	0.0	nd	0.8	0.1	nd	0.1
Al <sub>2</sub> O <sub>3</sub>	22.0	24.1	2.4	21.8	24.2	4.1	20.7	24.2	12.6	20.9	24.8	12.3	21.3	26.6	12.9
Cr <sub>2</sub> O <sub>3</sub>	0.2	nd	0.1	0.1	nd	0.1	0.0	nd	0.0	0.0	nd	0.1	0.0	nd	0.0
FeO	26.4	0.5	22.6	27.9	0.2	22.0	28.9	0.0	23.0	26.3	0.0	21.7	26.0	0.2	24.3
MnO	0.4	nd	0.1	0.5	nd	0.1	3.2	nd	0.6	1.9	nd	0.6	2.9	nd	0.5
MgO	10.0	nd	22.4	8.1	nd	23.2	2.9	nd	6.0	3.2	nd	6.3	2.1	nd	5.5
CaO	2.3	5.3	0.2	3.8	5.6	0.3	6.8	5.8	11.6	9.6	5.9	11.4	11.0	8.2	11.2
Na <sub>2</sub> O	0.0	8.9	0.0	0.0	8.3	0.0	0.0	8.2	1.0	0.0	8.6	1.0	0.0	7.1	1.1
K <sub>2</sub> O	0.0	0.1	0.0	0.0	0.2	0.0	0.0	0.1	1.3	0.0	0.1	1.0	0.0	0.1	1.0
Total	100.8	101.1	100.0	101.0	100.5	103.3	99.3	98.5	98.3	99.3	100.3	96.3	101.4	100.7	98.0
<i>P–T</i> estimates	8.6 kbar, 725 °C			12.9 kbar, 850 °C			9.2 kbar, 705 °C			11.4 kbar, 690 °C			9.7 kbar, 705 °C		

**Note:** Mineral abbreviations after Kretz (1983). Sample locations are as follows: 561b, 63°53.333'N, 92°38.130'W; 342, 63°52.552'N, 92°38.610'W; 178d, 63°51.478'N, 92°44.902'W; 201, 63°50.541'N, 92°41.237'W. nd, not detected.



**Fig. 5.** *P–T* results. (a) Mafic dyke (sample 98TXM342). Composition plot corresponds to Grt and Pl shown in SEM image. *P–T* plot shows results based on garnet core compositions. (b) Grt-bearing anorthositic gabbro (sample 99TXM561b). The dotted line (indicated in both the SEM image and the composition profile) roughly marks the interface between the low-CaO core and the high-CaO rim in Grt. The *P–T* plot, lower left, shows results for inner rim calculations. (c) Quartzofeldspathic (Qf) gneiss (sample 98TXM178d). Composition plot (lower right) corresponds to the Grt porphyroblast shown in the backscatter SEM image. Note the abrupt increase in CaO ( $X_{\text{Grs}}$ ) at the Grt rim in the composition profile (lower right) and SEM image (lower left). The *P–T* plot shows results for core calculations. (d) Amphibolite from south of the Uvauk complex anorthosite suite (sample 98TXM201). Composition plot (upper right) corresponds to the Grt porphyroblast shown in the SEM image. Note the marked increase in CaO content ( $X_{\text{Grs}}$ ) at the core–rim interface, demarcated by the dotted line. The *P–T* plot shows results based on rim compositions.



ilmenite, pyrite, rutile, monazite, and zircon. Anhedral garnet porphyroblasts range from 500  $\mu\text{m}$  to 1 mm in diameter, are wrapped by quartz veins and ribbons, and commonly contain quartz inclusions. Orthopyroxene is typically <100  $\mu\text{m}$  and generally occurs within garnet pressure shadows (Fig. 5c). Cumingtonite is randomly oriented, suggesting that it formed during retrograde breakdown of orthopyroxene (MacDonald 1999 and references therein). Fine-grained (20–50  $\mu\text{m}$ ) biotite is also randomly oriented within bands ~100  $\mu\text{m}$  thick. Plagioclase porphyroclasts range up to 1 mm in diameter and are mantled by subgrains.

Garnet compositional profiles (Fig. 5c) indicate low-CaO cores ( $X_{\text{Grs}} = 0.05\text{--}0.07$ ) and ~50–100  $\mu\text{m}$  wide high-CaO rims ( $X_{\text{Grs}} = 0.08\text{--}0.11$ ) that decrease outward to  $X_{\text{Grs}} = 0.06\text{--}0.08$  rims (Fig. 5c). Although locally diffuse, the generally abrupt increase in CaO suggests a two-stage (M1–M2) history akin to that inferred for the garnet leucogabbro within the northern shear zone. Fe/(Fe + Mg) increases more

gradually from cores (0.60–0.62) to rims (0.66–0.69). Plagioclase compositions vary between  $\text{An}_{21}$  and  $\text{An}_{29}$ , with no apparent relation between composition and textural location. Orthopyroxene is generally unzoned but locally exhibits a marked increase in Al and a slight decrease in Fe/(Fe + Mg) toward the rim. M1 conditions of 8.4 kbar and 725  $^{\circ}\text{C}$ , based on the average of three microdomains, were calculated using garnet cores and matrix orthopyroxene and plagioclase (Fig. 5c). M2a conditions of 11.4 kbar and 805  $^{\circ}\text{C}$  are based on garnet rims and matrix phases located proximal to garnet porphyroblasts.

#### Sample 98TXM201: banded garnet amphibolite

In wall rocks south of the Uvauk complex (Fig. 3), a lens of garnet-amphibolite gneiss, several metres wide, is structurally concordant with host tonalite orthogneiss. The amphibolite is well banded with alternating melanocratic and leucocratic layers ~2 cm in width. Dark bands comprise ~40%

hornblende, 30% garnet, 20% plagioclase, 10% quartz, and minor biotite. Leucocratic bands comprise ~60% plagioclase, 25% quartz, 10% garnet, 5% hornblende, and trace ilmenite, rutile, and pyrite. Pre-tectonic to syntectonic garnet porphyroblasts range from ~2 mm to ~1 cm in diameter, are highly fractured, and commonly contain large (0.1–0.5 mm in diameter) quartz inclusions. Some garnet porphyroblasts are surrounded by thin (~150  $\mu\text{m}$ ) discontinuous moats with an inner, ~50  $\mu\text{m}$  wide plagioclase zone, surrounded by a ~100  $\mu\text{m}$  wide hornblende zone (Fig. 5d).

Plagioclase compositions vary between  $\text{An}_{28}$  and  $\text{An}_{38}$ , with the most calcic compositions occurring 20–50  $\mu\text{m}$  from garnet. The CaO content of garnet increases from core ( $X_{\text{Grs}} = 0.19\text{--}0.20$ ) to rim ( $X_{\text{Grs}} = 0.26\text{--}0.32$ ), with some variability between grains. Two of the three analyzed garnet porphyroblasts (both ~3 mm in diameter) show an abrupt transition to ~150–200  $\mu\text{m}$  wide, high-CaO rims, whereas the third garnet (~4 mm diameter) exhibits a more continuous increase over a distance of ~600  $\mu\text{m}$ . Fe/(Fe + Mg) ratios are relatively consistent (0.83–0.85), with a minor increase to 0.87–0.93 at the extreme rims. Amphiboles generally range from Fe-tschermakite to Fe-tschermakitite hornblende (after Leake 1978).

M1  $P$ – $T$  conditions of 9.2 kbar and 705  $^{\circ}\text{C}$ , based on the average of three microdomains, were calculated using the compositions of garnet cores together with hornblende and plagioclase located no closer to garnet than 100  $\mu\text{m}$  (Fig. 5d). Maximum  $P$ – $T$  (M2a) conditions of 11.2 kbar and 695  $^{\circ}\text{C}$ , based on the average of three microdomains, derive from high-CaO garnet rims and hornblende and plagioclase located within 100  $\mu\text{m}$  of garnet.  $P$ – $T$  conditions of initial garnet breakdown (M2b) are 9.7 kbar and 705  $^{\circ}\text{C}$  based on garnet rim and coronitic plagioclase and hornblende compositions.

## Summary

Textural observations, chemical zoning, and  $P$ – $T$  calculations summarized in the previous sections are consistent with two metamorphic events (i.e., M1, M2). M1 is characterized by pre-tectonic, low-CaO garnet cores that record 9 kbar and 705  $^{\circ}\text{C}$  in southern wall rocks, 8.4 kbar and 725  $^{\circ}\text{C}$  in the southern shear zone, and 11.0 kbar and 760  $^{\circ}\text{C}$  in the northern shear zone. M2 is characterized by syntectonic to post-tectonic garnet growth that, in rocks also containing the earlier low-CaO M1 garnet, is manifest as high-CaO garnet rims. M2 occurred under upper-amphibolite- to granulite-facies conditions that reached maximum  $P$ – $T$  (M2a) conditions between 11.2 kbar and 695  $^{\circ}\text{C}$  (southern wall rock sample 98TXM201) and 14.7 kbar and 790  $^{\circ}\text{C}$  (Uvauk complex gabbro sample 98TXM561b). Highest M2a temperatures (865  $^{\circ}\text{C}$ ) are recorded by gabbro dykes within the Uvauk complex anorthosite suite, suggesting that they may have represented a significant local heat source. Samples from the northern shear zone (sample 99TXM561b) and within the anorthosite suite (gabbro dyke sample 98TXM342) indicate ~4.3 kbar decompression (M2b) under sustained high temperatures (775–800  $^{\circ}\text{C}$ ), whereas southern country rocks (symplectite in sample 98TXM201) record ~1.5 kbar decompression (M2b) at 705  $^{\circ}\text{C}$ . The clockwise M2  $P$ – $T$  paths recorded by these samples are characteristic of metamorphism in response to tectonic thickening, with differential

uplift of ~3 kbar (~9 km) across the southern shear zone. Lastly, M3 (not described here; see Mills 2001) is a post-tectonic, retrograde event (5.8–6.0 kbar and 625–695  $^{\circ}\text{C}$ ) thought to reflect intrusion of Paleoproterozoic (ca. 1.85–1.81 Ga) Hudson granite (Peterson et al. 2002).

## Geochronology

Geochronological data were collected to constrain protolith ages and the metamorphic history of the Uvauk complex. The data we report here supersede preliminary age determinations presented by Tella et al. (1994).

## Methods

U–Pb geochronological samples were prepared and analyzed at the Geological Survey of Canada in Ottawa. All samples collected were ~30 kg in weight and were crushed in a steel jaw crusher and pulverized in a disk mill grinder. Heavy mineral separates were concentrated using a Wilfley™ table and heavy liquid (methyl iodine; specific gravity = 3.3) separation procedures. Magnetic grains were removed from the mineral separate using a rare earth magnet, and the less magnetic portion was passed through a Frantz™ isodynamic separator at increasing magnetic strengths. The nonmagnetic populations were rerun at maximum amperage (1.8 A) with decreasing side slope angles. Zircon, monazite, and rutile grains were selected for analyses using a binocular microscope. Turbid and fractured grains, or those with inclusions or visible overgrowths, were avoided where possible. Grain selection was based primarily on morphology, although colour and size were taken into account in some cases. Representative populations, or analytical fractions, were isolated and photographed.

Samples were air abraded for between 1 and 10 h using a pyrite powder to remove the outer part of the zircon (Krogh 1982). Monazites were not abraded, and only one of three rutile fractions was abraded for 20 min to remove surficial impurities. Abraded zircons were photographed and weighed prior to dissolution and ion exchange chemistry. Measurement utilized image-analysis software designed to estimate the weight of a zircon based on its size and density (Matthews and Davis 1999). Zircons representing the fraction types analyzed were imaged using cathode luminescence (CL) and backscattered electron (BSE) techniques using a scanning electron microscope (SEM) to study the internal structure of representative zircon morphological types.

Zircon and monazite fractions were spiked with a mixed  $^{205}\text{Pb}/^{235}\text{U}/^{233}\text{U}$  tracer and dissolved in Teflon™ microcapsules (Parrish 1987). The chemical procedure followed for U and Pb extraction was similar to that described by Roddick et al. (1987). Pb and U were loaded separately onto Re filaments using silica gel. Analyses were conducted using a Finnigan-Mat 261 multicollector thermal ionization mass spectrometer in static mode. Error propagation methods were those of Roddick (1987). Linear regressions were calculated using a variation of the method of York (1969), and age errors are quoted at the 95% confidence level. Results for U–Pb isotopic analyses for the three samples dated are presented in Table 2.



### Sample 98TXM334b: leucogabbro mylonite

A sample of leucogabbro was analyzed (Fig. 3) to determine the magmatic age of the anorthosite suite. The leucogabbro comprises ~55%–60% plagioclase, 30%–35% clinopyroxene, and 10% garnet, with minor orthopyroxene and trace quartz, ilmenite, magnesio-hastingsite, actinolite, and biotite. The sample contains a very well developed L–S mylonite foliation, with large ( $> 5 \text{ cm} \times > 5 \text{ cm} \times < 0.5 \text{ cm}$ ), flattened aggregates of clinopyroxene, indicative of coarse grain size prior to deformation. A ~250  $\mu\text{m}$  wide garnet corona typically surrounds clinopyroxene, and a  $< 100 \mu\text{m}$  wide plagioclase moat commonly lies inboard of garnet coronae. The matrix is composed of fine-grained polycrystalline plagioclase.

Two morphological types of zircon were analyzed: (i) colourless, euhedral, prismatic grains that lack visible cores, have slightly resorbed tips, and have aspect ratios of  $> 3:1$  (comprising ~80%–90% of all zircons); and (ii) roughly equant, multifaceted, subrounded zircons (possibly fragments). BSE images of some zircons show subdued, low luminescent internal zoning parallel to crystal faces (Fig. 6), consistent with a magmatic origin (e.g., Pidgeon 1992). More commonly, zircons are internally homogeneous or display patchy internal zoning, as seen using CL imaging.

### Results

Nine zircon analyses (both single-grain and multigrain fractions) yield  $^{207}\text{Pb}/^{206}\text{Pb}$  dates between 2720 and 2636 Ma. A York-fit linear regression (York 1969; Roddick 1987) through six fractions (4–9, inclusive) yields an upper intercept of  $2711^{+5}_{-4}$  Ma and a lower intercept of  $1933 \pm 86$  Ma (Fig. 6), with a mean standard weighted deviation (MSWD) of 1.44. The upper intercept is interpreted as the age of magmatic crystallization, whereas the lower intercept age suggests a component of Paleoproterozoic Pb loss, renewed zircon growth, or cryptic recrystallization. Either Pb loss or recrystallization is more likely because no overgrowths were detected on the zircon grains. Significantly older  $^{207}\text{Pb}/^{206}\text{Pb}$  dates for multigrain fractions 1 and 2 are interpreted to reflect a component of inherited zircon in these analyses.

### Sample 92-RAL-12: mylonitic garnet anorthosite

At the western end of the Uvauk complex, garnet-bearing anorthosite forms centimetre- to metre-scale layers that have been mylonitized and locally folded along with adjacent mafic granulite (e.g., Fig. 4e). Garnet anorthosite collected from this locality contains three morphological types of zircon. All are cloudy white to translucent, with one group of large (150–200  $\mu\text{m}$ ) subhedral grains (12, 13, 18, 21), another group (14, 15, 16, 17) of rounded needles (aspect ratio ~5:2) commonly showing irregular thinning of the central parts of the grains, and a third group of granular aggregates (not analyzed). SEM imaging reveals generally unzoned internal structure. Titanite is present as (i) irregular yellow-brown grains, interstitial to garnet, with hourglass and spheroidal shapes; and (ii) equant, pale yellow grains with well-developed facets. Euhedral ruby red and black rutile is also present.

### Results

Analyses of spheroidal and faceted grains of titanite,

interpreted to be metamorphic in origin, form a single near-concordant population with a mean  $^{207}\text{Pb}/^{206}\text{Pb}$  age of  $1902 \pm 6$  Ma. Four analyses (14, 15, 16, 17) of elongate zircon yield discordant  $^{207}\text{Pb}/^{206}\text{Pb}$  ages between 1895 and 2023 Ma but do not define a single coherent age population. The range in age is interpreted to indicate inheritance of significantly older zircon, combined with recrystallization and (or) Pb loss. Four analyses of the zircon with subhedral to round morphologies (12, 13, 18, 21) yield discordant  $^{207}\text{Pb}/^{206}\text{Pb}$  ages with a more restricted range between 1905 and 1921 Ma (Fig. 7). A unique interpretation is difficult because of the complexity of the data. A possible age for the subhedral to round zircon is given by the two youngest grains (12 and 13), which have similar  $^{207}\text{Pb}/^{206}\text{Pb}$  ages and define a two-point discordia with an upper intercept of  $1908.5 \pm 1.7$  Ma (Fig. 7; chord 1), within error of the titanite age described previously. In this interpretation, the older ages of fractions 18 and 21 must include an inherited component, which may have affected to a lesser extent the age determined for fractions 12 and 13. A maximum age estimate for the subhedral to round zircon of

Ma is derived by linear regression of three of the four analyses (13, 18, 21; MSWD = 0.1). Fraction 12 falls below this regression line, consistent with recent Pb loss. Two rutile analyses yield  $^{207}\text{Pb}/^{206}\text{Pb}$  ages of  $1799 \pm 8$  and  $1831 \pm 3$  Ma. Given the ca. 1902 Ma titanite age and geochronological results from the nearby Kramanituur complex that indicate rapid cooling from peak metamorphism at ca. 1902 through rutile closure at ca. 1900 Ma (Sanborn-Barrie et al. 2001), our preferred interpretation is that the subhedral to round zircon analyses represent a ca. 1908 Ma metamorphic and deformation event, with inheritance from an Archean protolith.

### Sample 98TXM352: garnet-quartzofeldspathic gneiss

Garnet-quartzofeldspathic gneiss was collected from the southern shear zone (Fig. 3) to constrain the timing of granulite-facies metamorphism. The location, fabrics, and mineralogy of the sample are comparable to those of the ~2599 Ma sample dated by Tella et al. (1994) and C. Roddick and S. Tella (unpublished data). The rock comprises ~30% garnet, 40% plagioclase, 20% quartz, 5% biotite, <5% cummingtonite, and trace ilmenite, pyrite, rutile, monazite, and zircon. Compositional banding in the gneiss is defined by alternating feldspar-rich layers and thin layers with abundant biotite, cummingtonite, and opaque minerals.

Zircon and monazite were recovered from the sample. Three monazite morphological types were analyzed: (1) tabular, subangular crystals; (2) spherical, smooth crystals; and (3) equidimensional, angular grains or grain fragments (Fig. 8a). Zircon grains are predominantly multifaceted, spherical, clear, and colourless, with coarsely pitted surfaces; based on this morphology, they are interpreted as metamorphic (Fig. 8b). Rare fragments with concave surfaces, interpreted as overgrowths that had spalled off of the outside of zircon grains during mineral separation procedures, were isolated as a potentially younger phase of zircon growth.

CL and BSE images of zircons generally reveal simple internal compositional zoning, though a small proportion of grains have inherited cores (Fig. 8b). The majority of zircons are either homogeneous or possess weak, patchy internal zoning, consistent with metamorphic crystal growth or recrystallization.



**Table 2.** U–Pb analytical data for samples collected from the Uvauk complex.

Fraction <sup>a</sup>	Wt. (μg) <sup>b</sup>	U (ppm)	Pb* (ppm) <sup>c</sup>	Pb <sub>c</sub> (pg) <sup>d</sup>	Atomic ratios <sup>e</sup>					Apparent age (Ma)	
					<sup>206</sup> Pb	<sup>208</sup> Pb	<sup>206</sup> Pb	<sup>207</sup> Pb	<sup>207</sup> Pb	<sup>206</sup> Pb	<sup>207</sup> Pb
					<sup>204</sup> Pb	<sup>206</sup> Pb	<sup>238</sup> U	<sup>235</sup> U	<sup>206</sup> Pb	<sup>238</sup> U	<sup>206</sup> Pb
<b>Sample 98TXM334b (Z5822): Uvauk complex leucogabbro</b> (location: 63°51.644'N, 92°40.630'W)											
1. Z1a(12), nm1°, eu, pr, incl, co	24	104	73	333	259	0.36	0.5249±0.55	14.141±0.50	0.19537±0.24	2720	2787.9±7.8
2. Z1c(3), nm1°, eu, pr, incl, co	18	136	97	197	366	0.36	0.5304±0.13	14.130±0.42	0.19324±0.33	2743	2769.9±11.0
3. Z2a(12), nm0°, eu, pr, cl, co	28	95	64	311	293	0.32	0.5196±0.47	13.320±0.43	0.18592±0.22	2697	2706.4±7.3
4. Z5b(1), nm0°, fg, eq, cl, co	5	80	51	4	3 768	0.23	0.5195±0.10	13.308±0.13	0.18579±0.05	2697	2705.3±1.7
5. Z5c(1), nm0°, fg, eq, cl, co	6	120	77	5	3 991	0.24	0.5191±0.09	13.275±0.12	0.18547±0.05	2695	2702.4±1.5
6. Z2c(6), nm0°, eu, pr, cl, co	3	78	52	5	1 518	0.30	0.5178±0.14	13.215±0.16	0.18509±0.06	2690	2699.1±2.1
7. Z1b(4), nm1°, eu, pr, incl, co	32	69	47	105	694	0.34	0.5172±0.22	13.198±0.22	0.18508±0.11	2687	2698.9±3.5
8. Z4(2), nm0°, fg, sph, cl, co,	8	99	66	3	7 257	0.31	0.5172±0.10	13.174±0.12	0.18473±0.04	2688	2695.8±1.4
9. Z2b(4), nm0°, eu, pr, cl, co	18	139	92	9	7 688	0.33	0.5053±0.09	12.659±0.11	0.18172±0.04	2636	2668.6±1.5
<b>Sample 92RAL12 (2797): Uvauk complex garnet anorthosite</b> (location: 63°51.582'N, 92°44.983'W)											
10. T-A(7), nm10°, py, sro, tb	113	13	10	86	390	1.30	0.3413±0.11	5.476±0.30	0.11636±0.24	1897	1901.0±9.0
11. T-B(6), nm10°, py, cl, fr	57	17	12	61	349	1.23	0.3421±0.12	5.495±0.33	0.11652±0.26	1900	1903.0±9.0
12. Z-D(1), nm10°, co, tb, incl, sro, sub	10	734	253	24	5 965	0.12	0.3242±0.09	5.213±0.10	0.11661±0.03	1855	1905.0±1.0
13. Z-E(1), nm10°, co, tb, incl, ro, sub	16	964	332	25	12 923	0.07	0.3373±0.11	5.430±0.12	0.11677±0.03	1890	1907.0±1.0
14. Z-F(1), nm10°, co, tb, incl, ro, sub	7	727	257	94	1 168	0.09	0.3404±0.09	5.532±0.13	0.11786±0.08	1906	1924.0±3.0
15. Z-G(2), nm10°, co, tb, incl, ndl, sub	4	738	285	36	1 901	0.14	0.3546±0.08	6.092±0.11	0.12461±0.05	1989	2023.0±2.0
16. Z-H(1), nm10°, co, tb, incl, ndl, sro	5	576	215	42	1 414	0.10	0.3545±0.08	6.004±0.12	0.12285±0.07	1976	1998.0±2.0
17. Z-I(1), nm10°, co, tb, incl, el, sro	2	692	250	47	719	0.15	0.3319±0.09	5.306±0.18	0.11595±0.13	1870	1895.0±5.0
18. Z-J(1), nm10°, co, tb, incl, sro	14	729	280	29	7 208	0.19	0.3416±0.08	5.531±0.10	0.11742±0.03	1905	1917.0±1.0
19. R-K(12), nm10°, rd, cl, sub	84	6	2	8	1 206	0.00	0.3190±0.19	4.837±0.26	0.10996±0.22	1791	1799.0±8.0
20. R-L(12), nm10°, bk, op, sub	55	11	3	7	1 686	0.00	0.3263±0.10	5.036±0.12	0.11194±0.07	1825	1831.0±3.0
21. Z-M(1), nm10°, co, tb, incl, sro	15	1650	585	49	11 128	0.08	0.3432±0.08	5.569±0.10	0.11768±0.03	1902	1921.0±1.0
<b>Sample 98TXM352 (Z5949): garnet-quartzofeldspathic gneiss</b> (location: 63°51.316'N, 92°41.311'W)											
22. Z3b(1), dia, eq, sph, cl, co	10	69	38	5	4 264	0.12	0.4913±0.09	11.699±0.10	0.17270±0.04	2576	2584.0±1.8
23. Z5d(1), dia, fg, og, fr, cl, co	8	78	44	5	3 861	0.17	0.4896±0.10	11.619±0.12	0.17212±0.05	2569	2578.4±1.5
24. Z5e(1), dia, fg, og, cl, co	5	41	24	3	2 179	0.20	0.4858±0.16	11.499±0.10	0.17168±0.10	2552	2574.0±3.3
25. Z3a(1), dia, eq, sph, cl, co	6	88	51	16	966	0.25	0.4773±0.13	10.990±0.15	0.16698±0.08	2516	2527.6±3.0
26. Z5a(1), dia, fg, og, cl, co	9	69	39	27	608	0.23	0.4742±0.12	10.915±0.19	0.16694±0.14	2502	2527.2±4.8
27. Z4a(5), dia, eq, sph, cl, co	17	74	42	3	13 129	0.23	0.4730±0.09	10.799±0.12	0.16557±0.04	2497	2513.4±1.4
28. Z5b(1), dia, fg, og, cl, co	9	69	38	5	3 396	0.18	0.4701±0.09	10.653±0.10	0.16436±0.04	2484	2501.1±1.6
29. Z5c(1), dia, fg, og, fr, cl, co	18	36	20	4	4 162	0.21	0.4599±0.10	10.367±0.12	0.16351±0.05	2439	2492.3±1.7
30. M2b(1), 1.5 A, eq, py, cl	4	3905	5611	4	104 941	2.19	0.4945±0.09	11.934±0.11	0.17503±0.04	2590	2606.4±1.4
31. M5(1), 1.5 A, eq, dy, incl, fr	13	332	8179	7	17 644	58.00	0.4808±0.10	11.272±0.12	0.17002±0.05	2531	2557.9±1.6
32. M2a(1), 1.5 A, eq, py, cl	2	227	6278	3	4 216	66.30	0.4722±0.16	10.965±0.17	0.16842±0.05	2493	2542.0±1.8
33. M1(1), 1.5 A, irr, py, cl	15	296	5829	8	13 736	54.60	0.4068±0.10	8.184±0.12	0.14590±0.05	2200	2298.4±1.6

Table 2 (concluded).

Fraction <sup>a</sup>	Wt. (μg) <sup>b</sup>	U (ppm)	Pb* (ppm) <sup>c</sup>	Pb <sub>c</sub> (pg) <sup>d</sup>	Atomic ratios <sup>e</sup>					Apparent age (Ma)	
					<sup>206</sup> Pb	<sup>208</sup> Pb	<sup>206</sup> Pb	<sup>207</sup> Pb	<sup>207</sup> Pb	<sup>206</sup> Pb	<sup>207</sup> Pb
					<sup>204</sup> Pb	<sup>206</sup> Pb	<sup>238</sup> U	<sup>235</sup> U	<sup>206</sup> Pb	<sup>238</sup> U	<sup>206</sup> Pb
Sample 98TXM298b (Z5824): quartz-ribboned tonalitic mylonite (location: 63°51.624'N, 92°41.166'W)											
34. Z2a(1), dia, eq, sph, cl, co	11	83	46	4	6 234	0.15	0.4863±0.09	11.421±0.12	0.17032±0.04	2555	2560.8±1.4
35. Z3b(1), dia, eq, sph, cl, co	6	26	15	12	382	0.27	0.4824±0.32	11.300±0.30	0.16987±0.18	2538	2556.4±6.2
36. Z1b(1), dia, spr, cl, co	3	25	15	3	770	0.25	0.4850±0.28	11.301±0.73	0.16898±0.58	2549	2547.6±19.5
37. Z4b(1), dia, eq, sph, cl, co	3	49	28	34	150	0.20	0.4784±0.89	11.122±0.83	0.16862±0.50	2520	2544.0±16.8
38. Z3a(1), dia, eq, sph, cl, co	8	54	29	5	2 504	0.15	0.4789±0.10	11.053±0.13	0.16740±0.05	2522	2531.8±1.8
39. Z1a(1), dia, spr, cl, co	7	58	33	19	677	0.21	0.4763±0.19	10.939±0.23	0.16656±0.15	2511	2523.4±5.1
40. R1a(40), 0.5 A, fg, or, cl	44	0.61	0.16	38	28	—	0.2939±2.70	4.102±9.60	0.10123±8.2	1661	1647 <sup>+ 278</sup> <sub>- 341</sub>
41. R2a(35), 0.5 A, fg, bk, incl	198	0.15	0.04	61	23	—	0.2786±3.70	3.820±17.30	0.09945±15.1	1584	1614 <sup>+ 478</sup> <sub>- 705</sub>
42. R1b(40), 0.5 A, fg, rd, cl	79	0.65	0.16	89	25	—	0.2847±3.10	3.471±14.60	0.08842±12.7	1615	1392 <sup>+ 423</sup> <sub>- 587</sub>

<sup>a</sup>Mineral analyzed, followed by morphology type and the number (in parentheses) of grains included in the fraction: Z, zircon; T, titanite; R, rutile. Magnetic properties on Frantz™ magnetic separator: dia, diamagnetic at 1.8 A and -0.5° side slope; nm0°, nonmagnetic at indicated side slope in degrees. Grain characteristics: bk, black; cl, clear; co, colourless; dy, dark yellow; el, elongate; eq, equant; eu, euhedral; fg, fragment; fr, fractured; incl, inclusions; irr, irregular; ndl, needle; og, overgrowth; op, opaque; or, orange; pr, prismatic; py, pale yellow; rd, red; ro, rounded; sph, spherical; sro, subrounded; sub, subhedral; tb, turbid.

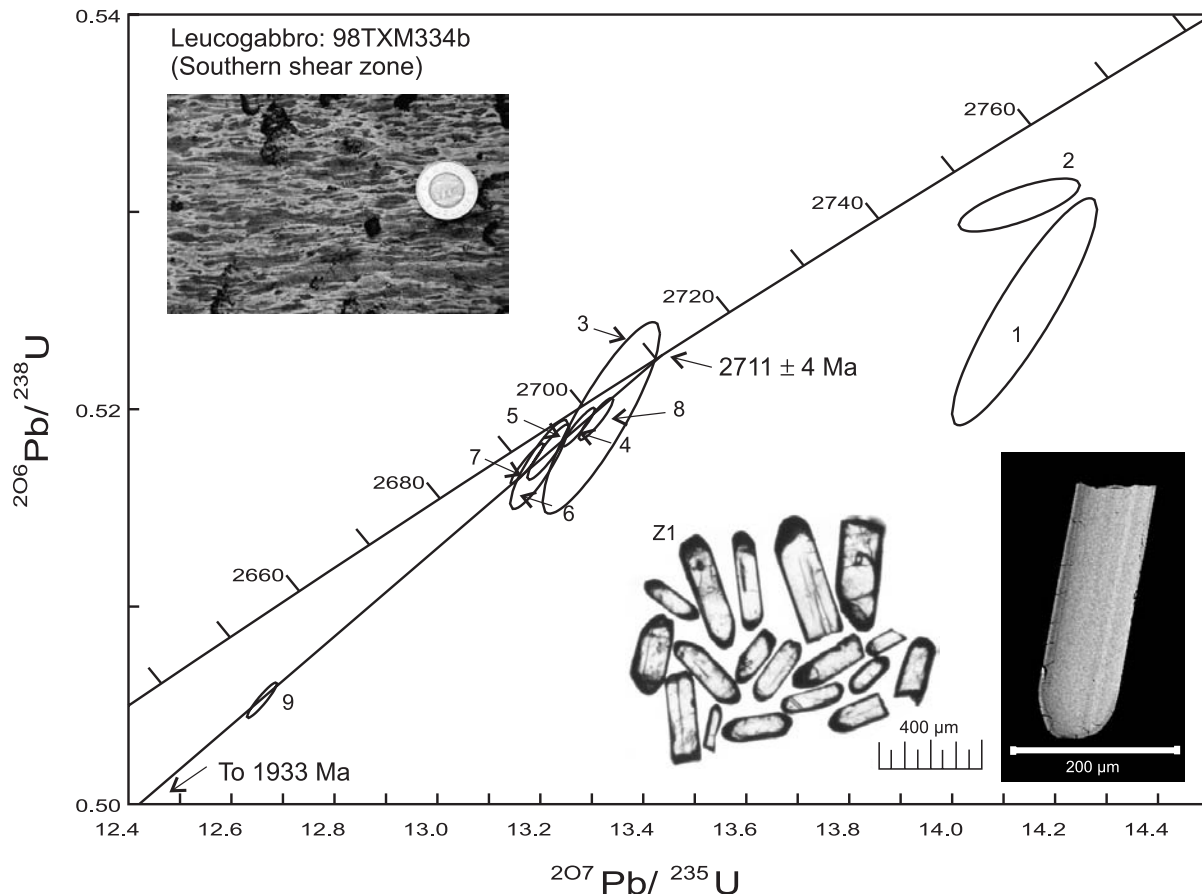
<sup>b</sup>Zircon fractions not weighed; weight estimated from grain size, therefore U and Pb concentration data are qualitative only. Concentration uncertainty varies with sample weight (>10% for sample weights <10  $\mu$ g and <10% for sample weights above 10  $\mu$ g).

<sup>c</sup>Total common Pb in analysis corrected for spike and fractionation.

<sup>d</sup>Radiogenic Pb.

<sup>e</sup>Atomic ratios corrected for spike, fractionation, blank and initial common Pb, except  $^{206}\text{Pb}/^{204}\text{Pb}$  ratio corrected for spike and fractionation only. Errors are 1s in %. Blank composition (atomic proportions):  $^{208}\text{Pb} = 0.5197$ ;  $^{207}\text{Pb} = 0.2136$ ;  $^{206}\text{Pb} = 0.2529$ ;  $^{204}\text{Pb} = 0.0139$ . Common Pb correction based on Cumming and Richards (1975) model.

**Fig. 6.** Concordia plot of U–Pb geochronology data of zircon from leucogabbro mylonite (sample 98TXM334b): upper and lower discordia chord intercepts are  $2711 \pm 4$  and  $1933 \pm 86$  Ma, respectively. Representative rock outcrop (coin for scale) and zircon grains of fraction Z1 are shown. SEM backscatter image shows prismatic crystal with rounded ends and faint zoning parallel to crystal faces, interpreted as magmatic zoning.



stallization (Pidgeon 1992; Mezger and Krogstad 1997). Most grains also possess  $\sim 10 \mu\text{m}$ , featureless overgrowths similar to those of zircons described from other granulite terrains (Hanchar and Rudnick 1995), and these appear bright in BSE images relative to the crystal interiors (Fig. 8b). Fragments, thought to be metamorphic overgrowths, exhibit a homogeneous internal structure.

## Results

### Monazite

Four single-grain analyses of monazite (one each of monazite type 1 and type 3 and two of type 2, as described earlier) are variably discordant (0.8%–5.0%) with  $^{207}\text{Pb}/^{206}\text{Pb}$  dates ranging between 2606 and 2298 Ma (Fig. 8a). Three of the fractions (excluding fraction 31) fall on a discordia chord with upper and lower intercepts of ca.  $2629 \pm 4.8$  and 1921 Ma (MSWD = 0.78; Fig. 8a), respectively, that are interpreted as end members of a mixed-age population. The upper intercept age may represent a metamorphic or igneous crystallization age for the sample. The lower intercept indicates either renewed metamorphic growth of monazite or recrystallization at ca. 1921 Ma. Monazite fraction 31 plots to the left of the discordia chord and is interpreted to record an earlier event affecting monazite, as also indicated in the zircon data presented in the next section.

### Zircon

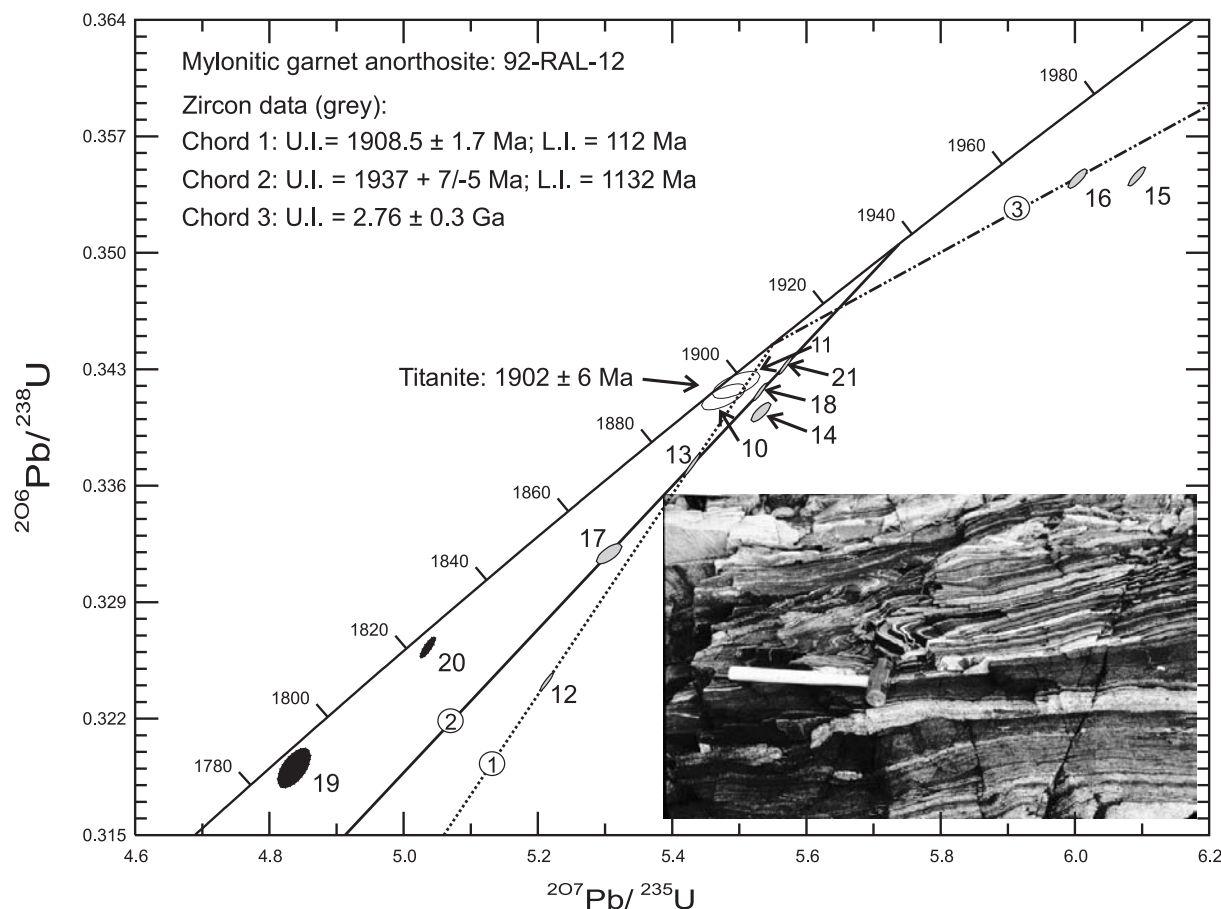
Eight analyses of both single and small, multigrain zircon fractions plot below concordia, with  $^{207}\text{Pb}/^{206}\text{Pb}$  dates between 2500 and 2600 Ma (Fig. 8b). Evidence of episodic zircon growth is provided by the thin ( $\sim 10 \mu\text{m}$ ) overgrowths apparent in BSE and CL images and the fact that fragments selected as overgrowths yield the youngest ages.

The spherical grains have a range of ages between 2530 and 2585 Ma, and these ages do not correlate with either grain size or Th and U contents (Fig. 8b). The three oldest analyses (21, 22, and 23) plot along a regression line with an upper intercept of  $2595 \pm 5$  Ma, pinned by a lower intercept of ca. 1900 Ma (chord 2 in Fig. 8b; MSWD = 1.7). The upper intercept (ca. 2595 Ma) is interpreted to represent a minimum age of early zircon growth, consistent with the interpretation of the monazite data. Fractions 25–29 plot to the left of (or above) this discordia chord and are interpreted to include a greater component of younger zircon. Although overgrowth material (i.e., the  $10 \mu\text{m}$  overgrowths) is likely to have been removed during the 5–10 h of abrasion of the spherical zircons, mixing of age components cannot be eliminated as the explanation for the range of ages between 2530 and 2595 Ma.

The two youngest zircon dates were determined from material selected as representative of overgrowths based on



**Fig. 7.** Concordia plot of U–Pb geochronology data for zircon (grey), titanite (unfilled), and rutile (black) from sample 92-RAL-12. Inset shows outcrop photograph of sample locality (hammer for scale). See text for discussion. L.I., lower intercept; U.I., upper intercept.



a negative crystal, cup-like morphology (27, 28). It remains uncertain, however, whether these overgrowth fragments are of the same generation as the relatively thin ( $\sim 10 \mu\text{m}$ ) overgrowths evident on most zircons from the quartzofeldspathic gneiss (Fig. 8b) or represent some other growth event. Additionally, it cannot be demonstrated that the analyzed overgrowth fragments are single-component material, as they may retain some portion of optically indistinguishable core material (e.g., 22 and 23). The least discordant overgrowth fragment has a minimum age of 2501 Ma (0.8% discordant). Assuming that the overgrowths were originally of a similar age, a discordia line through analyses 27 and 28 intersects the concordia curve at 2505 Ma (Fig. 8b), with a lower intercept of 733 Ma. Alternatively, if one assumes that the discordance in analysis 27 is entirely caused by an older event at ca. 1.9 Ga, as indicated earlier in the paper by the data for sample RAL-12, the lower intercept of the regression for sample 98TXM334b, and the monazite ages reported earlier, then the upper intercept date for fraction 28 is  $\sim 2530$  Ma. The possibility that the age of the overgrowths is younger than estimated earlier cannot be eliminated. For example, regression of the most concordant analyses (22, 23, 25, 27, 28) yields a line (chord 1, Fig. 8b) with upper and lower intercepts of  $2620 \pm 22$  and  $2319 \pm 323$  Ma, respectively (MSWD = 0.42). Based on regional considerations cited previously and discussed further later in the paper, however, this interpretation is not favoured.

In summary, the geochronological data are consistent with metamorphic growth or recrystallization of zircon and monazite at ca. 2595, zircon growth between 2505 and 2530 Ma, and zircon and monazite growth at ca. 1920 Ma.

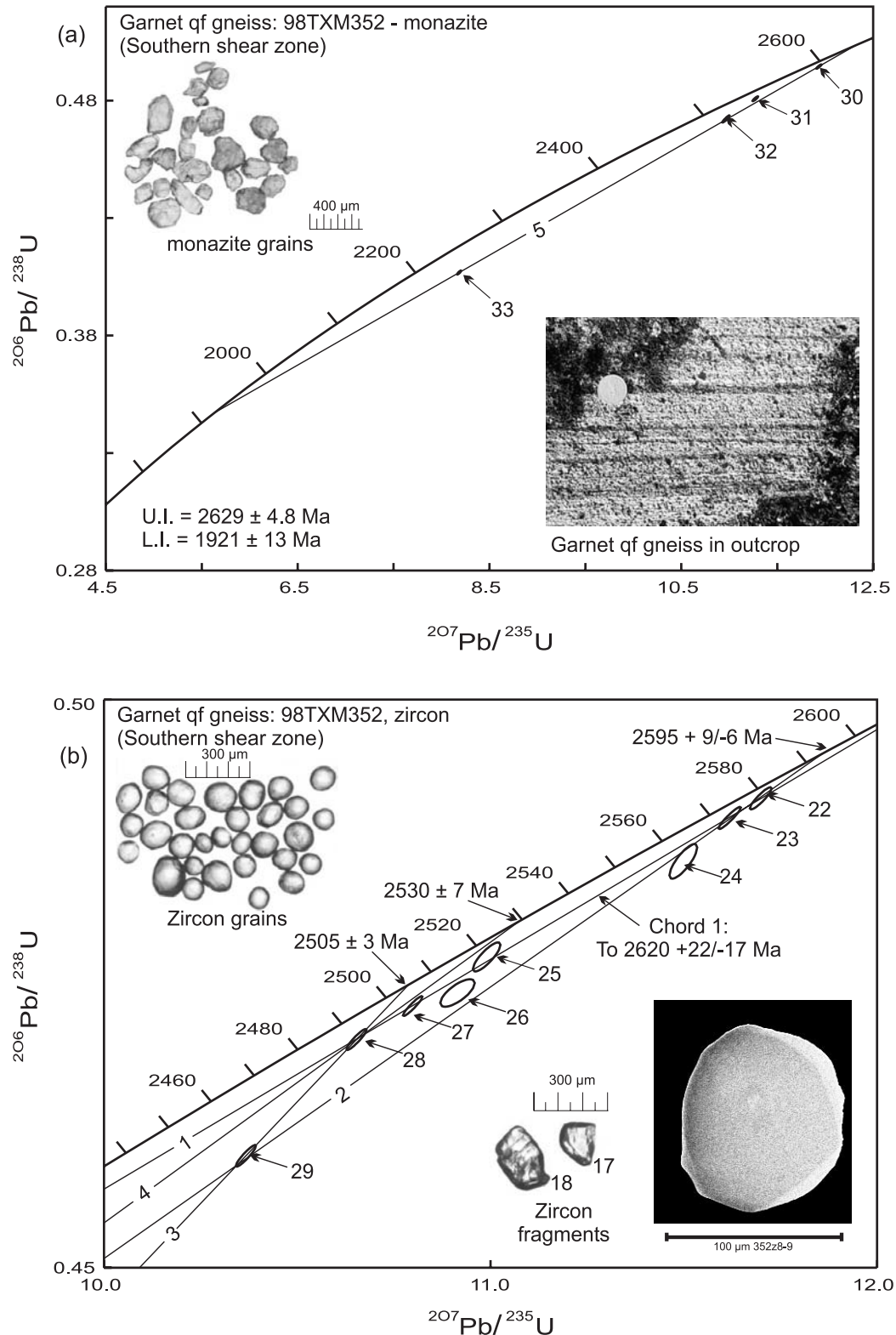
#### Sample 98TXM298b: tonalite ultramylonite

Within the southern shear zone, tonalitic ultramylonite (Fig. 9a) occurs in 10–50 cm thick sheets intercalated with dioritic mylonite and quartzofeldspathic gneiss and contains a granulite-facies assemblage consisting of plagioclase and quartz, with minor garnet and orthopyroxene. It is interpreted to have had a shared tectonothermal history with the quartzofeldspathic gneiss and was sampled to help constrain the timing of granulite-facies deformation within this shear zone. The rock is leucocratic, composed of up to 90% quartz and feldspar, with only  $\sim 5\%$  biotite, 3% orthopyroxene, 2% garnet, and trace hornblende, ilmenite, zircon, and rutile. Plagioclase porphyroclasts ( $< 2$  mm in diameter) make up  $< 10\%$  of the rock, and the matrix is composed of fine-grained ( $< 200 \mu\text{m}$ ) plagioclase interpreted to have formed by grain-size reduction during ductile deformation.

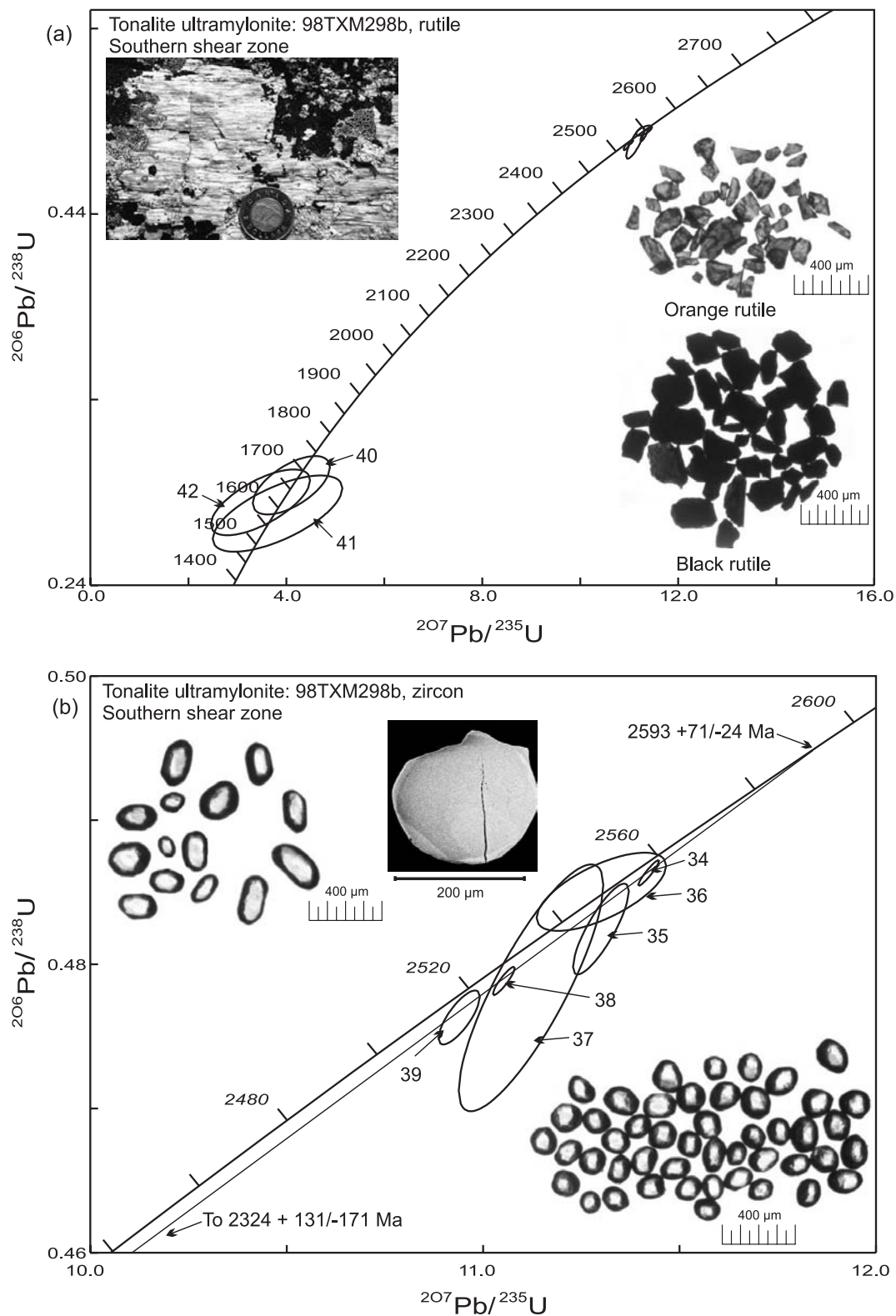
#### Results

Zircon and rutile were separated for geochronological analysis. Most zircons are nearly equant, ellipsoidal to spherical, and well faceted (Fig. 9b). Subhedral stubby prisms (aspect ratio  $< 3:1$ ) are also present. Zircons display thin ( $\sim 10 \mu\text{m}$ )

**Fig. 8.** Concordia diagrams for garnet quartzofeldspathic (qf) gneiss (sample 98TXM352). (a) Monazite data. Three of the four monazite fractions define a discordia chord with upper and lower intercepts of  $2629 \pm 4.8$  and  $1921 \pm 13$  Ma, respectively. Photographs of representative monazite grains and rock outcrop (coin for scale) are also shown. (b) Zircon data. Complexities in the dataset are discussed in the text; zircon fractions 28 and 29 are fragments thought to represent overgrowths and define a chord with upper intercept at  $2505 \pm 3$  Ma. SEM backscatter image in lower right corner shows zircon with homogeneous core and a thin ( $\sim 10 \mu\text{m}$ ) overgrowth.



**Fig. 9.** Concordia diagrams for Qtz-ribboned tonalite mylonite (sample 98TXM298b). (a) Rutile data show large error ellipses likely resulting from grains with very low concentrations of U and radiogenic Pb. Photograph of representative rock outcrop also shown (coin for scale). (b) Detail of upper concordia plot showing zircon data. Photographs of representative zircon morphologies are shown. SEM backscatter image reveals homogeneous zircon cores with thin rims, similar to zircons from the quartzofeldspathic gneiss.





**Table 3.** Summary of *P–T* and geochronology constraints for the Uvauk complex.

Lithology	Location	Sample No.	<i>P–T</i> <sup>a</sup>		Age (Ma)
			Peak	Postpeak	
Leucogabbro	Uvauk complex	98TXM334b			2711 <sup>+5</sup> <sub>–4</sub> (igneous; upper intercept, zircon)
<b>Plutonism and (or) M0 metamorphism</b>					
Quartzofeldpathic gneiss	South shear zone	98TXM352			2629±5 (igneous or metamorphic; upper intercept, monazite) 2595±5 (igneous or metamorphic; upper intercept, zircon)
<b>M1 metamorphism + deformation (?)</b>					
Tonalite mylonite	South shear zone	98TXM298b			2560–2530 (metamorphic; zircon)
Quartzofeldpathic gneiss	South shear zone	98TXM352			2530–2501 (metamorphic; upper intercept, zircon)
		98TXM178d	8.4 kbar, 725 °C		
Amphibolite wall rock	South wall rock	98TXM201	9.2 kbar, 705 °C		
Garnet leucogabbro	North shear zone	99TXM561b	11.3 kbar, 760 °C		
<b>M2 metamorphism + deformation</b>					
Garnet anorthosite	Uvauk complex	92RAL12			1908±2 (metamorphic; upper intercept, zircon) 1902±6 (cooling; titanite)
Leucogabbro	Uvauk complex	98TXM334b			1933±86 (metamorphic; lower intercept, zircon)
Quartzofeldpathic gneiss	South shear zone	98TXM352			1921±13 (metamorphic; lower intercept, monazite)
Gabbro dyke	Uvauk complex	98TXM342	12.7 kbar, 870 °C	8.8 kbar, 775 °C	
Quartzofeldpathic gneiss	South shear zone	98TXM178d	11.4 kbar, 805 °C		
Amphibolite wall rock	South wall rock	98TXM201	11.2 kbar, 695 °C	9.7 kbar, 705 °C	
Garnet leucogabbro	North shear zone	99TXM561b	14.7 kbar, 790 °C	10.0 kbar, 800 °C	
<b>Post-M3 metamorphism</b>					
Garnet anorthosite	Uvauk complex	92RAL12			1799±8; 1831±3 (cooling; rutile)
Tonalite mylonite	South shear zone	98TXM298b			1647–1392 (cooling; rutile)
Metapsammite	South wall rock	Mills 2001	5.9 kbar, 660 °C		

<sup>a</sup>Pressure–temperature values.

overgrowths with no discernible internal structure (Fig. 9b), suggesting that they are metamorphic in origin.  $^{207}\text{Pb}/^{206}\text{Pb}$  zircon ages range between 2530 and 2560 Ma, with many of the analyses less than 0.5% discordant. These results are similar to those for the adjacent sample described earlier and are interpreted to reflect episodic zircon growth or recrystallization between 2500 and 2600 Ma.

Rutile was selected for analyses based on colour and size. Large (up to 400  $\mu\text{m}$ ), black, vitreous grains and fragments are most common. Dark red to rust-coloured rutile fragments, some with dark ilmenite intergrowths, are next in abundance. Least common are deep orange to amber rutile fragments with ilmenite intergrowths that were physically removed by cracking the grains. Three multigrain rutile fractions, one of each of the populations described previously, yielded discordant  $^{207}\text{Pb}/^{206}\text{Pb}$  ages ranging from 1647 to 1392 Ma (Fig. 9a). The large error ellipses associated with these analyses result from the very low concentrations of U and radiogenic Pb (Table 1). The young  $^{207}\text{Pb}/^{206}\text{Pb}$  ages of rutile relative to the zircon ages reflect the significantly lower closure temperature of rutile relative to zircon (400 °C for rutile versus >800–900 °C for zircon; Heaman and Parrish 1991, and references therein; Cherniak and Watson 2001). The rutile data are interpreted to indicate that the rock last cooled below 400 °C at ca. 1650 Ma.

## Discussion

Thermobarometric and geochronologic data obtained in this study are summarized in Table 3. Petrological results point to two distinct metamorphic events involving metamorphism at moderately high  $P$  (M1) and high  $P$  (M2). Porphyroblast–fabric relationships indicate M2 was synchronous with mylonitic foliation development, but these relationships do not constrain whether or not deformation accompanied M1. Geochronological data reveal that, following ca. 2.71 Ga anorthosite magmatism, three main episodes of zircon–monazite growth occurred at ca. 2.62–2.60, 2.56–2.50, and 1.91 Ga, with the latter age corresponding to M2, based on regional correlation of the mafic dyke (sample 98TXM342), which experienced only the M2 event (see M2 discussion later in this section). The lack of correspondence between the number of metamorphic and zircon–monazite growth events makes it unclear whether M1 spanned the ca. 2.62–2.50 Ga period or whether evidence of a discrete, early, metamorphic episode (M0) was overprinted by the ca. 2.56–2.50 Ga episode. Given the evidence for ca. 2.61 Ga plutonism in the northwestern Hearne and Rae domains (Davis et al. 2006, and references therein), we consider it likely that the upper intercept ages of monazite (quartzofeldspathic gneiss) and zircon data (quartzofeldspathic gneiss and tonalite mylonite) reflect ca. 2.62–2.60 Ga plutonism within the Uvauk complex.

Upper intercepts of discordia lines through discordant zircon overgrowth fractions in quartzofeldspathic gneiss (ca. 2.53 and 2.50 Ga; sample 98TXM352) and the tonalite mylonite (ca. 2.53 and 2.56 Ga; sample 98TXM298b) may indicate discrete episodes of crystallization during a ca. 2.56–2.50 Ga metamorphic event, consistent with geochronological data obtained from the MacQuoid (Berman et al. 2000; Stern and Berman 2000) and Yathkyed (MacLachlan et al. 2005)

supracrustal belts in the northwestern Hearne subdomain to the southwest of the Uvauk complex (Fig. 2) and the southern shear zone of the Kramanitu complex (Sanborn-Barrie et al. 2001), as well as ca. 2.53 Ga ages recorded in mafic granulites from the east Athabasca mylonite zone (Baldwin et al. 2003; Flowers et al. 2006; Mahan et al. 2006). Similar to the interpretation applied to the MacQuoid belt (Berman et al. 2000), we correlate this event with M1 metamorphism recognized within the Uvauk complex as low-CaO garnet cores (in three of the four samples studied petrologically) recording  $P$ – $T$  conditions between 8.4 and 11.0 kbar and between 705 and 760 °C (Table 3).

Regional constraints (Berman et al. 2000; Stern and Berman 2000; MacLachlan et al. 2005) indicate that the ca. 2.56–2.50 Ga metamorphism in the northwestern Hearne subdomain was associated with regional deformation ( $D_2$ ). South of the Uvauk complex the regional event culminated in ca. 2.50 Ga development of the Big Lake shear zone (Ryan et al. 2000a, 2000b). This shear zone is interpreted as a southeast-directed thrust juxtaposing isotopically more evolved (Nd model ages between 2.8 and 3.0 Ga), >2.69 Ga tonalites of the Cross Bay complex (Fig. 2) with juvenile (2.63–2.73 Ga Nd model ages), ca. 2.68–2.66 Ga volcanic rocks and tonalites of the northwestern Hearne subdomain (Ryan et al. 2000a, 2000b). Although direct evidence of a ca. 2.5 Ga age for the mylonitic fabric in the southern shear zone at the Uvauk complex is lacking, a similar relationship is considered likely at the Uvauk complex with the southern shear zone placing ca. 2.71 Ga anorthositic rocks structurally above tonalitic footwall rocks that are considered correlative with tonalite of the northwestern Hearne subdomain. This scenario is supported by the additional correlation with the 2.55–2.52 Ga age determined for the southern shear zone of the Kramanitu complex, located 50 km west of the Uvauk complex. The occurrence of a folded mylonitic foliation on the western side of the Uvauk complex (Fig. 4e) is also consistent with, but does not prove, this scenario. Gently dipping foliations within rocks of the less deformed (see later in the paper) east side of the complex suggest an originally shallow geometry similar to that proposed for the Big Lake shear zone (Ryan 2000a, 2000b).

The age of the high- $P$  M2 event experienced by the Uvauk complex mafic dyke (sample 98TXM342) can be established through comparison of the Uvauk complex with the Kramanitu complex (Fig. 2) (Sanborn-Barrie et al. 2001). The latter is dominated by gabbro–anorthosite, garnet anorthosite, and gabbro dykes all recording peak  $P$ – $T$  of 12–14 kbar and 800–850 °C, followed by ~5 kbar of uplift recorded in symplectitic coronae. Geochronological data indicate anorthosite–gabbro magmatism contemporaneous with high- $P$  metamorphism at ca. 1901 Ma, followed by extremely rapid cooling through the rutile closure temperature at ca. 1898 Ma. Gabbro dykes at the Kramanitu and Uvauk complexes are similar with respect to lithology, relationship to host anorthosite and anorthositic gabbro, geochemical characteristics (Mills 2001), and near-peak  $P$ – $T$  recorded in a single-stage  $P$ – $T$  loop. This strong correspondence provides a link between the two complexes that supports a ca. 1.9 Ga age for M2 at the Uvauk complex (Table 3).

The M2 event at the Uvauk complex is interpreted to be

best constrained by the ca. 1908 Ma interpreted age of zircon within garnet anorthosite (sample 92RAL12), with cooling through titanite closure at  $1902 \pm 6$  Ma (Table 3). The single-stage metamorphic history of the gabbro dyke (sample 98TXM342) suggests Uvauk complex dyke emplacement at this time, providing a significant heat source during granulite-facies metamorphism that may have localized deformation. The clockwise M2  $P$ - $T$ - $t$  path recorded by samples inside and outside the Uvauk complex suggests an overall regime of crustal thickening, with regional M2 thickening that culminated with the intrusion of mafic magma, as was concluded for the Kramanituak complex (Sanborn-Barrie et al. 2001). Near-isoclinal folding (Fig. 4e) of the western part of the Uvauk complex into an east-plunging synform reflects a roughly north-south-shortening regime. This orientation of strained rocks, deformed at 1.9 Ga, is similar to that which produced ~5–6 kbar, Barrovian-style metamorphism and deformation at 1.885 Ga in the Josephine River belt on the south side of Chesterfield Inlet (Fig. 2) (Berman et al. 2002a). We speculate that the north-south-shortening regime at ca. 1.91–1.89 Ga was a response to early collisional events of the Trans-Hudson Orogen, thought to have involved accretion of microcontinents to the southeastern flank of the Rae domain (e.g., Berman et al. 2005).

In the Kramanituak complex, mafic magmatism was followed by rapid exhumation and cooling from ~12 kbar and 800 °C at ca. 1902 Ma to ~8 kbar and ~500 °C (U-Pb rutile) by 1901–1896 Ma (Sanborn-Barrie et al. 2001). In comparison, the Uvauk complex is interpreted to have cooled from ~865 °C at ca. 1908 Ma through ~650 °C titanite closure (Heaman and Parrish 1991; Scott and St-Onge 1995) at ca. 1902 Ma. The 11–14 kbar pressures calculated for samples within and south of the Uvauk complex are similar to pressures recorded within and north of the Kramanituak complex (Sanborn-Barrie et al. 2001), indicating that both make up part of a ca. 1.90 Ga high- $P$  block that extends beyond the boundaries of these complexes. Uplift and cooling of this block between ca. 1.90 and 1.83 Ga are thought to have been accomplished at least in part by northwest-vergent thrusting along the Chesterfield fault zone (Fig. 2) (Berman et al. 2002b). Uvauk complex rutile ages of ca. 1.60 Ga likely reflect cooling after resetting by ca. 1.83 Ga Hudson granite that intruded the central portion of the Uvauk complex (Tella et al. 1993). Consistent with this interpretation are ca. 1.80 Ga  $^{39}\text{Ar}/^{40}\text{Ar}$  hornblende ages from the Uvauk complex (H. Sandeman, unpublished data).

## Conclusions

Metamorphic and geochronologic data for the Uvauk complex indicate four important periods of tectonic activity, involving ca. 2.71 Ga anorthosite magmatism, ca. 2.62–2.60 Ga magmatism  $\pm$  tectonometamorphism, ca. 2.56–2.50 Ga tectonometamorphism at 9–11 kbar, and ca. 1.91–1.90 Ga tectonometamorphism at 11–14 kbar. Although offering support for the ca. 2.60 Ga tectonic activity within the Snowbird tectonic zone invoked by Hanmer (1997), these data clearly indicate that two younger metamorphic events were of prime importance and obscure the nature of the ca. 2.60 Ga event in the Uvauk complex. The evidence at the Uvauk complex for 2.56–2.50 Ga zircon and monazite growth complements

the ca. 2.55–2.52 Ga age of the southern shear zone of the Kramanituak complex (Sanborn-Barrie et al. 2001) and the 2.50 Ga age of the Big Lake shear zone (Ryan et al. 2000a, 2000b), suggesting that the Snowbird tectonic zone may have existed as a discrete ca. 2.56–2.50 Ga structure. Thus, while also offering strong support for recent studies indicating major thermal and structural reworking of the Snowbird tectonic zone at ca. 1.90 Ga (Sanborn-Barrie et al. 2001; Baldwin et al. 2003; Flowers et al. 2006), the Uvauk complex dataset underscores the polycyclic nature of the Snowbird tectonic zone.

## Acknowledgments

This work comprises the M.Sc. of Mills and was supported by funding from the Polar Continental Shelf Project to the western Churchill National Geoscience Mapping Program (NATMAP) project, Natural Sciences and Engineering Research Council of Canada grant 37234-1999 to RGB, and Carleton University, with analytical support provided by the Geological Survey of Canada. The authors gratefully acknowledge the efforts of Katherine Venance, who performed microprobe analyses, Pat Hunt, who helped with the use of the scanning electron microprobe, Mike Jackson, who prepared numerous thin sections, and Nancy Macdonald, Gillian Royle, and Mariska ter Meer, who all provided field assistance. The authors also thank Hamish Sandeman, Wouter Bleeker, and journal reviewer Pat Bickford for constructive reviews of various drafts of this manuscript.

## References

- Aranovich, L.Y., and Berman, R.G. 1997. A new garnet-orthopyroxene thermometer based on reversed  $\text{Al}_2\text{O}_3$  solubility in  $\text{FeO-Al}_2\text{O}_3\text{-SiO}_2$  orthopyroxene. *American Mineralogist*, **82**: 345–353.
- Baldwin, J.A., Bowring, S.A., and Williams, M.L. 2003. Petrological and geochronological constraints on high pressure, high temperature metamorphism in the Snowbird tectonic zone, Canada. *Journal of Metamorphic Geology*, **21**: 81–98.
- Baldwin, J.A., Bowring, S.A., Williams, M.L., and Williams, I.S. 2004. Eclogites of the Snowbird tectonic zone: petrological and U-Pb geochronological evidence for Paleoproterozoic high-pressure metamorphism in the western Canadian Shield. *Contributions to Mineralogy and Petrology*, **147**: 528–548.
- Berman, R.G. 1990. Mixing properties of Ca-Mg-Fe-Mn garnets. *American Mineralogist*, **75**: 328–344.
- Berman, R.G. 1991. Thermobarometry using multi-equilibrium calculations: a new technique, with petrological applications. *Canadian Mineralogist*, **29**: 833–855.
- Berman, R.G., and Aranovich, L.Y. 1996. Optimized standard state and mixing properties of minerals. I. Model calibration for olivine, orthopyroxene, cordierite, garnet, and ilmenite in the system  $\text{FeO-MgO-CaO-Al}_2\text{O}_3\text{-SiO}_2\text{-TiO}_2$ . *Contributions to Mineralogy and Petrology*, **126**: 1–24.
- Berman, R.G., Ryan, J.J., Tella, S., Sanborn-Barrie, M., Stern, R., Aspler, L., et al. 2000. The case of multiple metamorphic events in the Western Churchill Province: evidence from linked thermobarometric and in-situ SHRIMP data, and jury deliberations. *Geological Association of Canada – Mineralogical Association of Canada, Program with Abstracts*, **25**: 836.
- Berman, R.G., Davis, W.J., Ryan, J.J., Tella, S., and Brown, N., 2002a. In situ SHRIMP U-Pb geochronology of Barrovian facies-series metasedimentary rocks in the Happy Lake and Josephine



- River supracrustal belts: implications for the Paleoproterozoic architecture of the northern Hearne domain, Nunavut. *In* Radiogenic age and isotopic studies, report 15. Geological Survey of Canada, Current research 2002-F4. 14 p.
- Berman, R.G., Pehrsson, S., Davis, W.J., Snyder, D.B., and Tella, S. 2002b. A new model for ca. 1.9 Ga tectonometamorphism in the western Churchill Province: linked upper crustal thickening and lower crustal exhumation. Geological Association of Canada – Mineralogical Association of Canada, Program with Abstracts, **27**: 9.
- Berman, R.G., Sanborn-Barrie, M., Stern, R., and Carson, C. 2005. Tectonometamorphism at ca. 2.35 and 1.85 Ga in the Rae domain, western Churchill Province, Nunavut, Canada: insights from structural, metamorphic and *in situ* geochronological analysis of the southwestern Committee Bay belt. *Canadian Mineralogist*, **43**: 409–442.
- Cherniak, D.J., and Watson, E.B. 2001. Pb diffusion in zircon. *Chemical Geology*, **172**: 5–24.
- Cumming, G.L., and Richards, J.R. 1975. Ore lead isotope ratios in a continuously changing Earth. *Earth and Planetary Science Letters*, **28**(2):155–171.
- Davis, W.J., Hanmer, S., Aspler, L., Sandeman, H., Tella, S., Zaleski, E., et al. 2000. Regional differences in the Neoarchean crustal evolution of the western Churchill Province: can we make sense of it? Geological Association of Canada – Mineralogical Association of Canada, Program with Abstracts, **25**: 864.
- Davis, W.J., Hanmer, S., Aspler, L., Tella, S., Sandeman, H., and Ryan, J. 2006. U–Pb geochronology of the MacQuoid supracrustal belt and Cross Bay plutonic complex: key components of the northwestern Hearne subdomain, Western Churchill Province, Nunavut, Canada. *Precambrian Research*, **145**: 53–80.
- Flowers, R., Bowring, S.A., and Williams, M.L. 2006. Timescales and significance of high-pressure, high-temperature metamorphism and mafic dike anatexis, Snowbird tectonic zone, Canada. *Contributions to Mineralogy and Petrology*, **151**: 558–581.
- Fuhrman, M.L., and Lindsley, D.H. 1988. Ternary-feldspar modeling and thermometry. *American Mineralogist*, **73**: 201–215.
- Gibb, R.A., and Halliday, D.W. 1974. Gravity measurements in southern District of Keewatin and southeastern District of Mackenzie, N.W.T. Energy, Mines and Resources Canada, Earth Physics Branch, Ottawa, Gravity Map Series 124-131.
- Gordon, T.M. 1988. Precambrian geology of the Daly Bay area, District of Keewatin. Geological Survey of Canada, Bulletin 422.
- Hanchar, J.M., and Rudnick, R.L. 1995. Revealing hidden structures: the application of cathodoluminescence and back-scattered electron imaging to dating zircons from lower crustal xenoliths. *Lithos*, **36**: 289–303.
- Hanmer, S. 1997. Geology of the Striding–Athabasca mylonite zone, northern Saskatchewan and southeast District of Mackenzie. Geological Survey of Canada, Bulletin 501.
- Hanmer, S. 2000. Granulite-facies microstructure of the Striding–Athabasca mylonite zone, western Canada: phase dispersion, brittle deformation, and elongate porphyroblasts. *Journal of Structural Geology*, **22**: 947–967.
- Hanmer, S., and Williams, M.L. 2001. Targeted fieldwork in the Daly Bay Complex, Hudson Bay, Nunavut. *In* Current research, part C. Geological Survey of Canada, Paper 2001-C15.
- Heaman, L., and Parrish, R.R. 1991. U–Pb geochronology of accessory minerals. *In* Applications of radiogenic isotope systems to problems in geology. Edited by L. Heaman and J.N. Ludden. Mineralogical Association of Canada, Short Course 19, pp. 59–102.
- Hoffman, P.F. 1988. United plates of America, the birth of a craton: early Proterozoic assembly and growth of Laurentia. *Annual Review of Earth and Planetary Sciences*, **16**: 543–603.
- Holland, T., and Blundy, J. 1994. Non-ideal interactions in calcic amphiboles and their bearing on amphibole–plagioclase thermometry. *Contributions to Mineralogy and Petrology*, **116**: 443–447.
- Kretz, R. 1983. Symbols for rock-forming minerals. *American Mineralogist*, **68**: 277–279.
- Krogh, T.E. 1982. Improved accuracy of U–Pb zircon dating by creation of more concordant systems using an air abrasion technique. *Geochimica et Cosmochimica Acta*, **46**: 637–645.
- Leake, B.E. 1978. Nomenclature of amphiboles. *Canadian Mineralogist*, **16**: 501–520.
- MacDonald, N. 1999. A comparative study of microstructural development in amphibolite- and granulite-facies mylonites of the Uvauk complex, Kivalliq region, Nunavut. B.Sc. thesis, Carleton University, Ottawa, Ont.
- MacLachlan, K., Davis, W.J., and Relf, C. 2005. U/Pb geochronological constraints on Neoarchean tectonism: multiple compressional events in the northwestern Hearne domain, western Churchill Province, Canada. *Precambrian Research*, **42**: 85–109.
- Mäder, U.K., Percival, J.A., and Berman, R.G. 1994. Thermobarometry of garnet–clinopyroxene–hornblende granulites from the Kapuskasing structural zone. *Canadian Journal of Earth Sciences*, **31**(7): 1134–1145.
- Mahan, K.H., Williams, M.L., and Baldwin, J.A. 2003. Contractional uplift of deep crustal rocks along the Legs Lake shear zone, western Churchill Province, Canadian Shield. *Canadian Journal of Earth Sciences*, **40**(8): 1085–1110.
- Mahan, K.H., Goncalves, P., Williams, M., and Jercinovic, M. 2006. Dating metamorphic reactions and fluid flow: application to exhumation of high-P granulites in a crustal-scale shear zone, western Canadian Shield. *Journal of Metamorphic Geology*, **2**: 385–388.
- Matthews, W., and Davis, W.J. 1999. A practical image analysis technique for estimating the weight of abraded mineral fractions used in U–Pb dating. *In* Radiogenic age and isotopic studies, report 12. Geological Survey of Canada, Current research 1999-F, pp. 1–7.
- McMullin, D.W., Berman, R.G., and Greenwood, H.J. 1991. Calibration of the SGAM thermobarometer for pelitic rocks using data from phase-equilibrium experiments and natural assemblages. *Canadian Mineralogist*, **29**: 889–908.
- Mezger, K., and Krogh, E.J. 1997. Interpretation of discordant U–Pb zircon ages: an evaluation. *Journal of Metamorphic Geology*, **15**: 127–140.
- Mills, A. 2001. Tectonometamorphic investigation of the Uvauk complex, Nunavut, Canada, M.Sc. thesis, Carleton University, Ottawa, Ont.
- Newton, R.C. 1983. Geobarometry of high-grade metamorphic rocks. *American Journal of Science*, **283A**: 1–28.
- Parrish, R.R. 1987. An improved micro-capsule for zircon dissolution in U–Pb geochronology. *Chemical Geology, Isotope Geoscience Section*, **66**: 99–102.
- Peterson, T.D., Van Breeman, O., Sandeman, H., and Cousens, B. 2002. Proterozoic (1.85–1.75 Ga) igneous suites of the Western Churchill Province: granitoids and ultrapotassic magmatism in a reworked Archean hinterland. *Precambrian Research*, **119**: 73–100.
- Pidgeon, R.T. 1992. Recrystallisation of oscillatory zoned zircon: some geochronological and petrological implications. *Contributions to Mineralogy and Petrology*, **110**: 463–472.
- Roddick, J.C. 1987. Generalized numerical error analysis with applications to geochronology and thermodynamics. *Geochimica et Cosmochimica Acta*, **51**: 2129–2135.

- Roddick, J.C., Loveridge, W.D., and Parrish, R.R. 1987. Precise U/Pb dating of zircon at the sub-nanogram Pb level. *Chemical Geology*, **66**: 111–121.
- Ross, G.M., and Eaton, D.W. 2002. Proterozoic tectonic accretion and growth of western Laurentia: results from Lithoprobe studies in northern Alberta. *Canadian Journal of Earth Sciences*, **39**(3): 313–329.
- Ross, G.M., Milkereit, B., Eaton, D., White, D., Kanasevich, E.R., and Burianyk, J.A. 1995. Paleoproterozoic collisional orogen beneath the western Canada sedimentary basin imaged by Lithoprobe crustal seismic-reflection data. *Geology*, **23**: 195–199.
- Ryan, J., Davis, W., Berman, R., Sandeman, H., Hanmer, S., and Tella, S. 2000a. 2.5 Ga granulite-facies activity and post-1.9 Ga low-grade reactivation along the Big lake shear zone, MacQuoid–Gibson lakes area (Nunavut): a fundamental boundary in the western Churchill Province. *Geological Association of Canada – Mineralogical Association of Canada, Program with Abstracts*, **25**: 924.
- Ryan, J.J., Hanmer, S., Sandeman, H.A., and Tella, S. 2000b. Archean and Paleoproterozoic fault history of the Big lake shear zone, MacQuoid–Gibson lakes area, Nunavut. *In* Current research, part C. Geological Survey of Canada, Paper 2000-C6. pp. 1–12.
- Sanborn-Barrie, M., Carr, S.D., and Thériault, R. 2001. Geochronological constraints on metamorphism, magmatism and exhumation of deep-crustal rocks of the Kramanituar complex, with implications for the Paleoproterozoic evolution of the Archean western Churchill Province, Canada. *Contributions to Mineralogy and Petrology*, **141**: 592–612.
- Schau, M. 1991. Orthogneiss, paragneiss, and high strain zones on northeast Coats Island, District of Keewatin, NWT. *In* Current research, part C. Geological Survey of Canada, Paper 91-1C, pp. 195–203.
- Scott, D.J., and St-Onge, M.R. 1995. Constraints on Pb closure in titanite based on rocks from the Ungava Orogen, Canada: implications for U–Pb geochronology and *P–T–t* path determination. *Geology*, **23**: 1123–1126.
- Stern, R.A., and Berman, R.G. 2000. Monazite U–Pb and Th–U geochronology by ion microprobe, with application to in situ dating of an Archean metasedimentary rock. *Chemical Geology*, **172**: 113–130.
- Tella, S., and Annesley, I.R. 1988. Hanbury Island shear zone, a deformed remnant of a ductile thrust, District of Keewatin, N.W.T. *In* Current research, part C. Geological Survey of Canada, Paper 88-1C, pp. 283–289.
- Tella, S., and Schau, M. 1994. Geology, Gibson Lake (east-half), District of Keewatin, Northwest Territories. Geological Survey of Canada, Open File 2737.
- Tella, S., Schau, M., Armitage, A.E., and Loney, B.C. 1993. Precambrian geology and economic potential of the northeastern parts of Gibson Lake map area, District of Keewatin, Northwest Territories. *In* Current research, part C. Geological Survey of Canada, Paper 93-1C, pp. 197–208.
- Tella, S., Schau, M., Roddick, J.C., and Mäder, U. 1994. Significance of juxtaposed mid-crustal mylonite zones of contrasting ages, Uvauk Complex, central Churchill Province, District of Keewatin, NWT, Canada. *Geological Society of America, Abstracts with Programs*, **26**: 135.
- Walcott, R.I., and Boyd, J.B. 1971. The gravity field of northern Alberta, and part of Northwest Territories and Saskatchewan, with maps. Energy, Mines and Resources Canada, Earth Physics Branch, Gravity Map Series 103-111. 13 p.
- York, D. 1969. Least squares fitting of a straight line with correlated errors. *Earth and Planetary Science Letters*, **5**: 320–324.